IPPT Reports on Fundamental Technological Research
1/2026

The Latest Scientific Achievements of the Institute of Fundamental Technological Research

Institute of Fundamental Technological Research
Polish Academy of Sciences

The Latest Scientific Achievements of the Institute of Fundamental Technological Research

IPPT Reports on Fundamental Technological Research

Institute of Fundamental Technological Research
Polish Academy of Sciences

Warsaw

IPPT Reports on Fundamental Technological Research
1/2026

The Latest Scientific Achievements of the Institute of Fundamental Technological Research

Edited by Daria Jóźwiak-Niedźwiedzka

Institute of Fundamental Technological Research
Polish Academy of Sciences

Warsaw 2026

Reviewers:
dr inż. Michał Batsch
prof. Maciej Bodnicki
prof. Elżbieta Jastrzębska
prof. Łukasz Kotwica
dr Magdalena Luty-Błocho
prof. Danuta Matykiewicz
prof. Agnieszka Ślosarczyk

Proofreading:
Ewa Kiczko

Graphic design cover:
Eliza Jezierska

ISSN 2299-3657
ISBN 978-83-65550-67-5 (print)
ISBN 978-83-65550-68-2 (online)
DOI: https://doi.org/10.24423/9788365550682

Institute of Fundamental Technological Research Polish Academy of Sciences
(Instytut Podstawowych Problemów Techniki Polskiej Akademii Nauk (IPPT PAN))
Pawińskiego 5B, 02-106 Warsaw
Phone 48 22 826 60 22, e-mail: reports@ippt.pan.pl
https://reports.ippt.pan.pl

Typesetting in LaTeX: Katarzyna Jezierska
Printed in Poland by: EXDRUK, Rysia 6, 87-800 Włocławek, Poland

Contents

Preface

The present volume, *The Latest Scientific Achievements of the Institute of Fundamental Technological Research*, highlights the most recent accomplishments of researchers at the Institute of Fundamental Technological Research of the Polish Academy of Sciences (IPPT PAN). It provides insight into cutting-edge studies that combine creativity, cross-disciplinary collaboration, and technological applicability in pursuit of scientific and societal progress.

The collected chapters reflect the broad thematic spectrum of research conducted at IPPT PAN – from novel methods of polymer waste valorisation and physicochemical modification of cement-based composites to micromechanics, microfluidics, and advanced metrology. What unites these contributions is a shared commitment to developing efficient engineering processes, promoting sustainable materials, and advancing modern experimental and numerical techniques.

The first chapter presents research on reusing PVC waste and transforming it into functional electrospun membranes for the removal of organic dyes from aqueous solutions. The proposed approach merges the principles of circular economy with the development of advanced filtration technologies.

The second chapter focuses on the application of power ultrasound treatment in the preparation of cement-based composites. The author emphasizes the potential of physical activation processes to enhance reactivity and durability, offering new perspectives for designing environmentally sustainable building materials.

In the third chapter, the authors describe a laboratory test rig for efficiency measurements of spur gear transmissions in micro-drive systems. This work supports the advancement of compact mechatronic devices by deepening the understanding of energy losses and load behaviour in small-scale mechanical systems.

The fourth chapter is devoted to the fabrication and characterization of thick chromium atomic force microscopy probes. The study demonstrates the advantages of metallic AFM probes with improved hardness and wear resistance, enabling precise measurements under demanding mechanical conditions.

Finally, the fifth chapter presents research on two-phase flow patterns in microfluidic cross-junctions, where a novel "bi-modal" droplet formation mode was identified. This discovery expands our understanding of hydrodynamic phenomena in microscale systems and opens new possibilities for applications in diagnostics and material engineering.

The presented studies illustrate the diversity and excellence of research conducted at IPPT PAN, reaffirming the Institute's role as a leading centre integrating fundamental science with technological innovation. The results showcased in this volume exemplify the Institute's ongoing development and the dedication of its researchers to addressing current scientific and societal challenges.

The Editorial Board extends sincere gratitude to all Authors for their valuable contributions and collaboration, as well as to the Reviewers for their constructive feedback, which has significantly improved the quality of this publication.

Daria Jóźwiak-Niedźwiedzka
Editor-in-Chief, IPPT Reports

Warsaw, March 2026

1. Reuse of PVC Waste and Its Transformation into Functional Electrospun Membrane to Remove Organic Dyes from Aqueous Solutions

Katarzyna Prus[1], **Aleeza Khurram**[2], **Emilia Karpiel**[2],
Paulina Pietrzyk-Thel[1], **Sławomir Wilczewski**[3*],
Marianna Gniadek[4], **Adrianna Nowak**[1], **Agata Roszkiewicz**[1],
Njemuwa Nwaji[1], **Justyna Widera-Kalinowska**[2],
Michael Giersig[1], **Magdalena Osial**[1*]

[1] Institute of Fundamental Technological Research, Polish Academy of Sciences
Warsaw, Poland
[2] Department of Chemistry, Adelphi University
Garden City, NY, USA
[3] Faculty of Chemical Technology and Engineering,
Bydgoszcz University of Science and Technology
Bydgoszcz, Poland
[4] Faculty of Chemistry, University of Warsaw
Warsaw, Poland
[*] Corresponding Authors: slawomir.wilczewski@pbs.edu.pl, mosial@ippt.pan.pl

The membrane technology in water treatment and desalination offers great potential in thin-film composite nanofiltration. This study utilized the electrospinning approach to fabricate nanofibers from recycled plasticized and unplasticized poly(vinyl chloride) (PVC) as a membrane for effective wastewater purification. The physicochemical properties and purification performance of the membranes were investigated. The obtained membrane showed potential as an adsorbent for cationic dyes in water. The pH-dependent study revealed optimal activity at pH of 7.0 for crystal violet (CV) and pH of 10 for methyl violet (MV) with plasticized PVC (PVC-P) showing enhanced ability compared to unplasticized PVC (PVC-R). Additionally, PVC-P shows a dye removal efficiency of 80 % and 55 % for CV and MV, respectively. Thus, the study could serve as an innovative dual-purpose approach to recycling spent PVC-based materials and wastewater treatment. The thermogravimetric analysis and tensile tests revealed that PVC-R fibers exhibited higher thermal stability ($T_{\mathrm{onset}} \approx 282\,^{\circ}\mathrm{C}$) and tensile strength ($\sim$10.6 MPa) compared to PVC-P fibers, while PVC-P fibers showed greater elasticity (elongation at break ∼40 %) but lower thermal resistance ($T_{\text{onset}} \approx 250\,^{\circ}\text{C}$). These results highlight the distinct structural behavior of rigid and plasticized PVC fibers under thermal and mechanical stress.

Keywords: PVC waste, adsorption, recycling, crystal violet, methyl violet, electrospun fibers.

https://doi.org/10.24423/9788365550682.ch1

Symbols and abbreviations

20/100/PVC-P – membrane based on PVC-P obtained at conditions: 20 kV and 100 µL min^{-1},
20/150/PVC-P – membrane based on PVC-P obtained at conditions: 20 kV and 150 µL min^{-1},
23/100/PVC-P – membrane based on PVC-P obtained at conditions: 23 kV and 100 µL min^{-1},
23/150/PVC-P – membrane based on PVC-P obtained at conditions: 23 kV and 150 µL min^{-1},
20/100/PVC-R – membrane based on PVC-R obtained at conditions: 20 kV and 100 µL min^{-1},
20/150/PVC-R – membrane based on PVC-R obtained at conditions: 20 kV and 150 µL min^{-1},
23/100/PVC-R – membrane based on PVC-R obtained at conditions: 23 kV and 100 µL min^{-1},
23/150/PVC-R – membrane based on PVC-R obtained at conditions: 23 kV and 150 µL min^{-1},
C_0 – initial concentration of dye solution [$\text{mol} \cdot \text{dm}^{-3}$],
C_x – concentration of the dye after adsorption [$\text{mol} \cdot \text{dm}^{-3}$],
CV – crystal violet,
DINP – diisononyl phthalate,
DMF – dimethylformamide,
$H\%$ – adsorption effectiveness,
k – adsorption rate constant,
k_1 – adsorption rate constants for the pseudo-first-order kinetic model,
k_2 – adsorption rate constants for the pseudo-second-order kinetic model,
KNO_3 – potassium nitrate,
m – mass of adsorbent [g],
MV – methyl violet,
NaCl – sodium chloride,
NaOH – sodium hydroxide,
pH_{ZPC} – pH at zero point of charge,
PVC-R – unplasticized PVC,
PVC-P – plasticized PVC,
R^2 – correlation coefficient,
SEM – scanning electron microscopy,
THF – tetrahydrofuran,

t – time [s],
TGA – thermogravimetry,
T_{onset} – onset temperature,
Q_e – amount of adsorbate at equilibrium,
Q_t – amount of adsorbate at a time t,
UV-vis – ultraviolet-visible light,
V – volume [dm^{-3}].

1. Introduction

Poly(vinyl chloride) (PVC) is an extensively utilized thermoplastic polymer widely used in daily life for its performance, including chemical and weathering resistance. Additionally, its broad use leads to the generation of post-consumer and post-process waste. This waste can be reprocessed; however, conventional mechanical and thermal recycling routes face important constraints arising from the diversity of formulation additives that affect processing and define end-use properties. Repeated reprocessing is further hindered by the inherently low thermal stability of PVC leading to partial or even extensive degradation, requiring moderation of the processing conditions. These limitations motivate the development of innovative methods for PVC reuse. Solvent-based dissolution emerges as a promising complementary route, as it enables the removal of low-molecular-weight additives from polymer blends and/or targeted re-modification of their properties [1–4].

The service performance of PVC strongly depends on the presence of plasticizers and other modifiers. Unplasticized PVC (PVC-R) is a rigid, durable, chemically resistant and UV-resistant polymer, widely used in building products such as window frames, water pipes, fencing, and other industrial applications. Plasticized PVC (PVC-P) incorporates low-molecular-weight plasticizers that reduce interchain interactions, improving flexibility and low-temperature performance. PVC-P is typically used in cable insulations, automotive interiors, floor coverings, and coating layers [1, 5]. Depending on additives such as plasticizers the recycling of PVC remains challenging and requires a change of experimental conditions during processing. Dissolution of PVC as a complementary recycling technique allows the use of other techniques, including electrospinning which enables fibrous structures fabrication. However, in the case of PVC, the process is limited by the low solubility of the polymer in typical organic solvents and the relatively high viscosity of its solutions. Previous studies on the electrospinning of poly(vinyl chloride) were concerned with the pristine polymer and focused primarily on the selection of solvent and their mixtures (mainly DMF and THF) [6], as well as on the optimization of electrospinning parameters such as the polymer concentration, applied voltage, and flow rate of the solution in order to obtain uniform nanofibers with the desired diameter [7, 8]. Electrospinning also enables incorporation of other ingredients such as plasticizers or other organic materials, e.g. PVP and/or inorganic fillers, e.g. MWCNTs [9], silver and titanium dioxide [10] to modify physicochemical characteristics of the material, including adsorptive properties.

The obtained PVC fibers were characterized by a large specific surface area, flexibility, and good dielectric properties, which create prospects for their application in insulations and filtration technologies [11, 12].

In this work, we present results on the use of electrospinning in the recycling of plasticized and unplasticized PVC waste to fabricate fibrous membranes to be used in water purification. Membranes were used to remove cationic dyes such as crystal violet and methyl violet 2B which are emerging contaminants affecting ecosystems [13–15] from aqueous solutions. Besides that, thermal and mechanical properties were examined. Unlike previously reported studies focused mainly on the electrospinning of pristine or modified PVC with synthetic fillers, the present research introduces a novel approach that utilizes both aged unplasticized (PVC-R) and plasticized (PVC-P) post-consumer wastes as precursors for electrospun nanofibrous membranes. This dual-purpose strategy simultaneously addresses the challenges of PVC recycling and the development of efficient, low-cost adsorptive materials for wastewater treatment, which has not been previously reported in the literature.

2. Experimental

2.1. Chemicals and methods

Poly(vinyl chloride) nanofibers were produced from a blend of unplasticized PVC S61 (Anwil S.A., Włocławek, Poland) with the following composition: Poly(vinyl chloride) PVC Neralit 601 100 phr, Organotin Patstab 2310 2 phr, Calcium stearate Ceasit I 1.2 phr, Fatty acid ester Loxiol G-32 1.5 phr, Acrylic-based polymer Poraloid K-125 1 phr, Acrylic-based polymer Poraloid K-175 1 phr, Paraffin Naftolube FTP 0.5 phr. Diisononyl phthalate (Sigma-Aldrich) was used as a plasticizer. Tetrahydrofuran (Sigma-Aldrich) and Dimethylformamide (Sigma-Aldrich) were used to prepare PVC solutions. Crystal violet, methyl violet, KNO_3, and NaOH were supplied by Warchem Sp. z o.o., Warsaw, Poland. HCl was supplied from POCH, Gliwice, Poland. Water was purified using HYDROLAB water filtering system, HYDROLAB, Gliwice, Poland.

Tensile properties were determined on strips 50 mm in length, 10 mm in width, and 0.06 ±0.005 mm in thickness (gauge length 30 mm). Measurements were performed on a Zwick/Roell Z010 testing machine (Ulm, Germany) at 23 °C, with a crosshead speed of 10 mm/min. Thermogravimetric analysis (TGA) was performed using a TG 209 F3 device (Netzsch Group, Germany) in the temperature range from 30 °C to 600 °C at a heating rate of 10 °C/min under a nitrogen atmosphere. The morphology of electrospun PVC-based materials was studied using Scanning Electron Microscopy (SEM), Merlin, Carl Zeiss, Stuttgart, Germany. The contact angle was measured using the Ossila L2004 goniometer by placing 1 µL of distilled water onto the PVC-P and PVC-R materials. The measurement was performed 20 times, with each droplet placed in a different location on the material. The pH was measured with the Elmetron CP-411 pH-meter. The UV-vis spectrometer Lambda1050+ (PerkinElmer) was used to measure the adsorption effectiveness. Determination of the functional groups in the materials was performed using the SpectrumTwo ATR (Perkin Elmer), while the Thermogravimetric Analyzer (TGA) TG8000 (Perkin Elmer) was used to determine the thermal stability of the materials. UV-vis, ATR, and TGA were supplied by the Pro-Environment Sp. z o.o., Warsaw, Poland.

2.2. Procedures

2.2.1. Preparation and aging of poly(vinyl chloride)

Unplasticized poly(vinyl chloride), also called rigid PVC (PVC-R), samples were prepared by extrusion and pressing. PVC was extruded using the co-rotating twin-screw extruder EHP-2x24 M (Zamak Mercator Ltd.) at a maximum temperature of 185 °C. Then, the material was granulated and pressed using a hydraulic press. The pressing process parameters were: temperature 190 °C, pressure 100 bar, time 5 min. Plates with dimensions of 120 × 120 × 2 mm were obtained. Plasticized PVC (PVC-P) plates were prepared by mixing the PVC dry blend with a diisononyl phthalate (DINP), which is a widely used plasticizer in PVC materials production (50 phr) at 110 °C for 2 h. The prepared blend was extruded and pressed in the same way as unplasticized PVC, but the maximum extrusion temperature was 165 °C, and the pressing temperature was 170 °C. The obtained materials were subjected to photodegradation and thermal aging (exposure to UV radiation and high temperature of 70 °C for 500 h).

2.2.2. Methodology of electrospinning of PVC

To produce electrospun PVC nanofibers, the polymer plates obtained after accelerated degradation were ground and dissolved in a THF/DMF mixture (1:1 w/w), producing 20 % PVC-R and PVC-P solutions, respectively. Electrospinning was carried out on a custom-built apparatus under the following parameters: voltages of 20 kV and 23 kV, flow rates of 100 µL min^{-1} and 150 µL min^{-1}, the needle-to-collector distance of 10 cm. Electrospinning was performed on a fixed metal plate covered with aluminum foil, using 5 mL of solution for each sample. The materials were labeled as follows: for nanofibers obtained at 20 kV and 150 µL min^{-1} from unplasticized PVC, the sample designation was 20/150/PVC-R. Similarly, samples obtained under 23 kV and 150 µL min^{-1}, 20 kV and

100 µL min^{-1}, 23 kV and 100 µL min^{-1} were labeled as 23/150/PVC-R, 20/100/PVC-R, 23/100/PVC-R, respectively. PVC-P samples were labeled in the same way, using PVC-P abbreviation: 20/150/PVC-P, 23/150/PVC-P, 20/100/PVC-P, and 23/100/PVC-P.

3. Results

3.1. Selection of electrospinning parameters for aged rigid and soft PVC

The selection of appropriate electrospinning parameters for plasticized and rigid PVC was based on thermal analysis and mechanical properties of the obtained fibrous mats. Table 1 shows thermal stability, tensile strength, and elongation at break for fibers obtained under all tested electrospinning conditions. As can be seen, depending on the experimental conditions during the electrospinning, samples are characterized by different mechanical properties. The highest thermal stability, tensile strength, and resistance to stretching among PVC-R and PVC-P samples show 23/150/PVC-R and 20/100/PVC-P samples.

Table 1. Thermal stability and mechanical properties of PVC-R and PVC-P fibers obtained under different electrospinning conditions.

Electrospinning parameter	T_{onset} [°C]	Tensile strength [MPa]	Elongation at tensile strength [%]
20/100/PVC-R	277.7 ±0.5	10.5 ±1.8	1.4 ±0.1
20/150/PVC-R	279.9 ±0.3	6.3 ±1.9	1.1 ±0.3
23/100/PVC-R	270.6 ±0.7	6.8 ±1.7	1.4 ±1.2
23/150/PVC-R	282.0 ±0.2	10.6 ±1.8	1.8 ±0.3
20/100/PVC-P	249.7 ±0.9	4.0 ±0.8	39.6 ±6.4
20/150/PVC-P	236.4 ±1.0	1.9 ±0.5	34.7 ±3.7
23/100/PVC-P	235.8 ±2.1	2.5 ±0.1	34.8 ±3.0
23/150/PVC-P	228.5 ±3.4	2.7 ±1.1	40.4 ±5.8

Figures 1a and 1b present the TGA curves and tensile curves, respectively, for materials obtained under the most favorable electrospinning conditions. Thermal analysis revealed that PVC fiber degradation followed the typical two-stage pattern for this polymer. The first stage, associated with polymer dehydrochlorination, occurred between ~150 °C and 325 °C. The second stage, between 350 °C and 425 °C, corresponds to carbon-based chain degradation. PVC-R exhibits higher thermal stability than PVC-P, which relates to the presence of plasticizer that changes durability and mechanical properties of the material [16–19]. In PVC-R, an additional degradation stage was observed up to ~125 °C, which

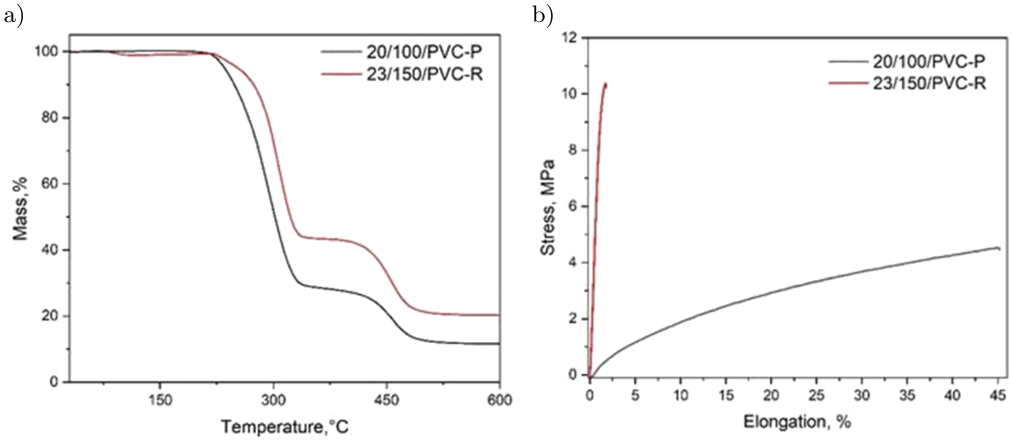

Fig. 1. a) TGA curves, and b) stress change as a function of elongation of PVC-R and PVC-P fiber-based membranes.

is assigned to solvent residue evaporation. This stage was absent in PVC-P, suggesting strong binding of the plasticizer to the polymer [20, 21]. Due to solvent residues, found mainly in PVC-R samples, the extrapolated onset temperature (T_{onset}) was used as a measure of thermal stability. Based on the analysis, the most favorable electrospinning conditions for aged PVC-R were 23 kV and 150 µL min^{-1}, and for PVC-P, 20 kV and 100 µL min^{-1}.

Figure 1b shows the tensile curves, and the tensile strength and elongation at break for electrospun mats from PVC-P and PVC-R, which are presented in Table 1. PVC-R samples showed significantly higher tensile strength, reaching 10.6 MPa for 23/150/PVC-R, but low elongation at break (~2 %), which is indicative of high stiffness and brittleness for this material. The sharp increase in stress at low strain suggests limited ability of PVC-R fibers to reorganize and undergo plastic deformation before failure. PVC-P samples displayed the opposite trend, reaching the maximum tensile strength of 4.0 MPa (20/100/PVC-P) and elongation at break of ~40 % [22, 23]. The gradual increase in stress with strain and the absence of a clear yield point are characteristic of materials with high flexibility and chain mobility. The results confirm that the presence of plasticizer significantly modifies the mechanical properties of PVC-based electrospun mats, increasing deformability of the material. The applied plasticizer was strongly bound to the polymer chain and did not migrate into the solvents, as evidenced by the mechanical properties typical of plasticized PVC [20, 24].

These results indicate that the selection of electrospinning parameters for aged PVC fibers should be matched to the polymer type and application requirements. For the tested PVC blends, the most favorable parameters were 23 kV and 150 µL min^{-1} for PVC-R, and 20 kV and 100 µL min^{-1} for PVC-P. Further studies were carried out using materials produced under these conditions.

3.2. Morphology and contact angle measurements

Morphology studies using the Scanning Electron Microscopy (SEM) clearly show differences between the PVC-P and PVC-R, indicating a key role of the plasticizer in the electrospinning of the fibrous membrane. In Fig. 2a PVC-P-based material reveals a textile-like structure made of micron-sized fibers that stack to each other forming flat, tight and highly porous membranes. The lack of plasticizer in the PVC-R sample caused a much looser structure made of much thicker fibers compared to the PVC-P. The images presented in Fig. 2b illustrate distilled water droplets onto PVC-P and PVC-R samples, where differences in the contact angle are seen. The contact angle for PVC-R is about 94.36 ±2.58, PVC-P is about 84.81 ±3.99. These values are much lower than the contact angle presented in the literature for the PVC-based electrospun fibers [25], which can be caused by different fibers morphology. Lower values result in more effective wetting of the membrane that can work not only as the mechanical barrier for the particle-based water pollutants but also as the adsorbent.

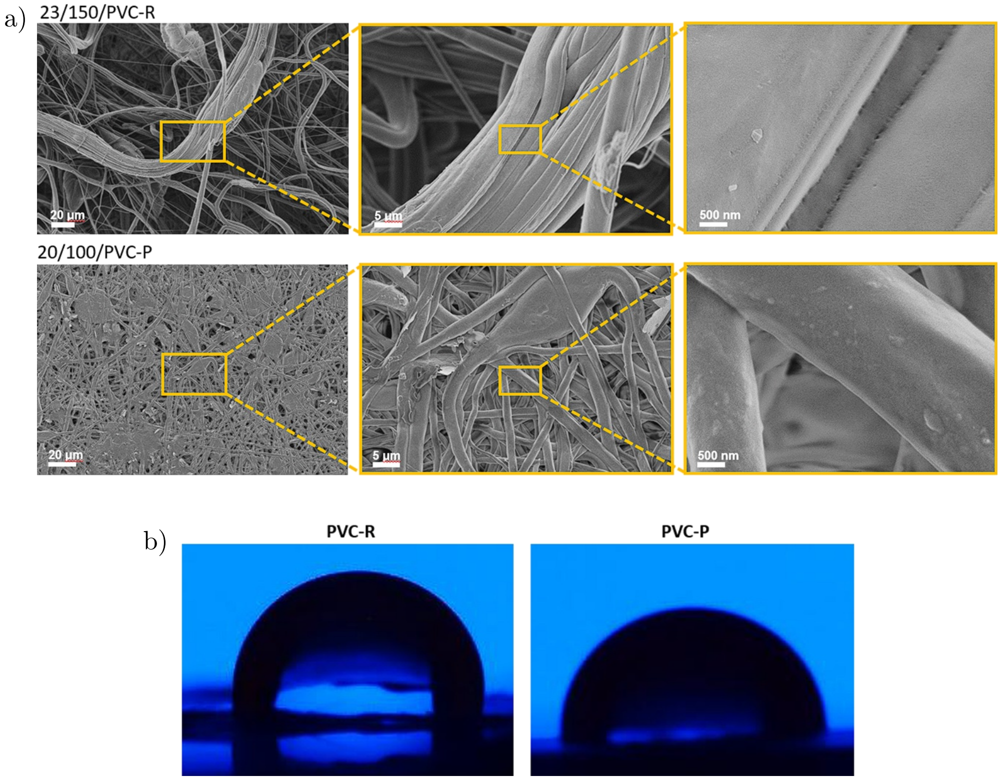

Fig. 2. a) SEM images, and b) images from the contact angle measurement for 23/150/PVC-R and 20/100/PVC-P.

3.3. Adsorption studies

The proposed electrospun membranes based on the recycled PVC were tested as adsorbents on dye-based organic pollutants. First, the point of zero charge (pH_{ZPC}) was measured to determine the affinity of the proposed membranes to cationic or anionic dyes. Measurements were performed in 0.05 M KNO_3, where 30 mg of both materials, PVC-R and PVC-P, were added to the 30 mL of solution, and the pH change after 24 h was recorded; pH was set using HCl and NaOH. As can be seen in Fig. 3a, the isoelectric point is about 5.92 for PVC-R and 5.82 for

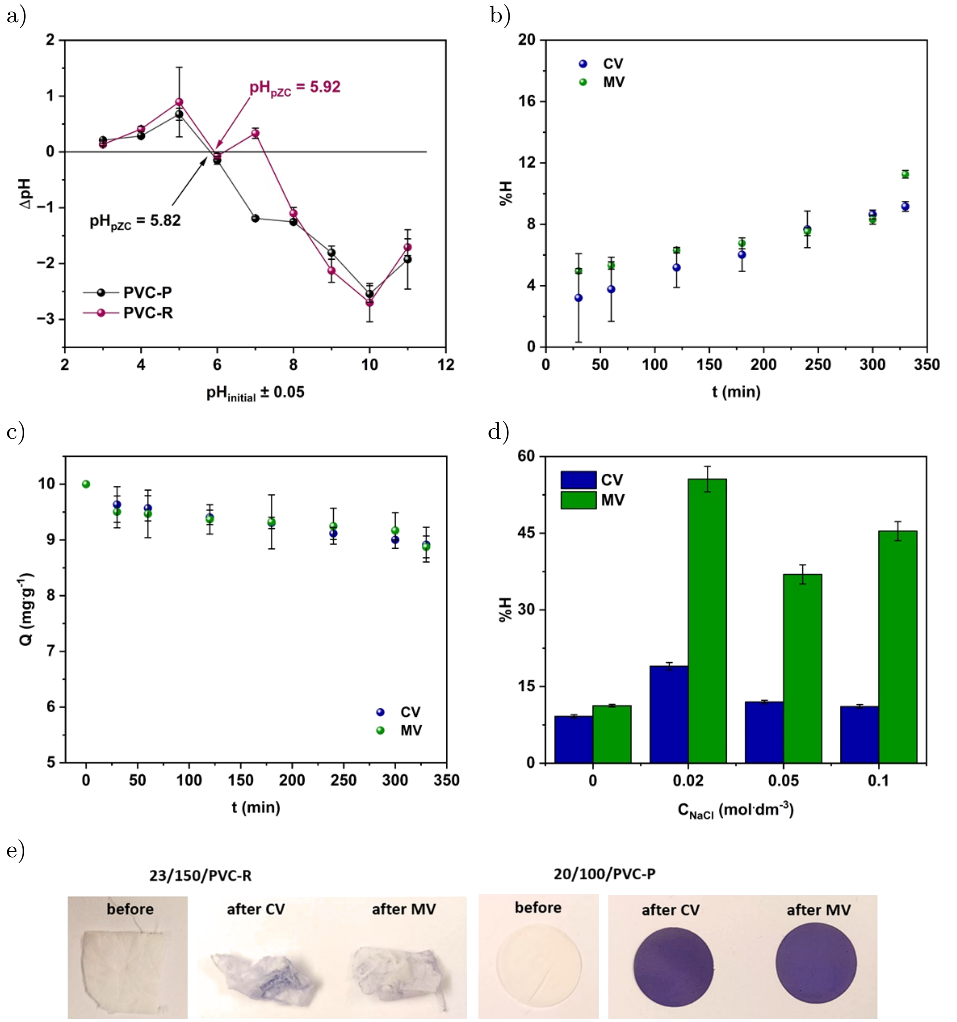

Fig. 3. a) pHPZC study for both materials (20/100/PVC-R and 23/150/PVC-P), adsorption effectiveness of CV and MV 20/100/PVC-R: b) as a function of time at pH 8.0, c) change of the dye concentration as a function of time, d) in different ionic strength moderated with NaCl.

PVC-P, while positive charge occurs below pH_{ZPC} and negative charge appears in the alkali media. The obtained values are similar to the pH_{ZPC} presented in the literature for PVC-based microplastics that may contain different additives, e.g., 5.8 [26], 6.43 [27]. A similar trend is recorded for both PVC-R and PVC-P-based materials. Therefore, cationic dyes, in particular crystal violet (CV) and methyl violet 2B (MV), were chosen as model pollutants in adsorption studies for the negative charge appearance onto membranes in the alkali media. As can be seen, the PVC-P may adsorb cationic dyes even in the neutral pH, while for PVC-R the surface may have a positive charge, which can affect cationic dyes removal in neutral pH.

The adsorption studies were performed using 10 ppm of both CV and MV dyes, where 30 mg of adsorbents, 23/150/PVC-R and 20/100/PVC-P, were added to 30 mL of CV and MV solutions. Then, the solution was mixed using a magnetic stirrer (250 rpm) for the uniform wetting of the fibrous membrane in the solution. Importantly, PVC-P samples tend to wet more effectively than PVC-R ones but undergo disassembly under mixing into separate fibers that can relate to the lower contact angle after the plasticizer introduction into the PVC-R. The adsorption effectiveness ($H\%$) was estimated using Eq. (1) [28]:

$$H\% = \frac{C_0 - C_x}{C_0} \times 100\,\%, \tag{1}$$

where C_0 is an initial concentration of dye solution [$\mathrm{mol \cdot dm^{-3}}$]; C_x stands for the concentration of the dye after adsorption [$\mathrm{mol \cdot dm^{-3}}$].

The adsorption effectiveness reaches just ∼8 % for CV removal and similarly ∼10 % for MV as seen in Fig. 3b. Moreover the change of dye concentration during the adsorption process also was not effective (Fig. 3c). However, with increasing ionic strength the effectiveness of adsorption processes was improving: for concentration of $0.02\,\mathrm{mol \cdot dm^{-3}}$ the $H\%$ removal of MV is about 60 %, while for CV about 15 %. Therefore, increasing NaCl concentration in the solution causes a decrease in the effectiveness of the adsorption process to ∼45 % for MV and ∼10 % for CV, respectively. Importantly, the PVC-R-based membrane changes its texture in the solution into fibrous, making it difficult to remove from the aqueous solutions. Figure 3e shows both 20/100/PVC-P and 23/150/PVC-R samples before and after the CV and MV treatment, where the removal effectiveness is clearly seen through the different coloration with dyes. The increase in ionic strength even worsened the texture, so for the following adsorption effectiveness studies at various pH the 20/100/PVC-P sample was chosen.

The adsorption capacity during the time (Q_t) was estimated using Eq. (2) [28] as follows:

$$Q_t = \frac{(C_0 - C_x) \times V}{m}, \tag{2}$$

where C_0 – initial concentration of dye solution [$\mathrm{mol \cdot dm^{-3}}$], C_x – concentration of the dye after adsorption [$\mathrm{mol \cdot dm^{-3}}$], V – volume [$\mathrm{dm^{-3}}$], m – mass of adsorbent [g].

Complementary to the spectrophotometric analysis, both types of membranes were investigated with FTIR before and after the adsorption of CV and MV to confirm the effectiveness of adsorption. First, bare 23/150/PVC-R and 20/100/PVC-P materials were compared to ascribe the peaks that are related to the presence of plasticizer in the material. Figure 4a shows normalized T% spectra, where the peaks located around (608, 637, 699, and 741) $\mathrm{cm^{-1}}$ can be ascribed to the C–Cl vibration in the PVC chain and/or peaks at 699 $\mathrm{cm^{-1}}$ and 741 $\mathrm{cm^{-1}}$ can come from the out-of-plane and in-plane aromatic ring bending, respectively. The following peak at 951 $\mathrm{cm^{-1}}$ relates to ν(C–H) vibration in CH_2 of the alkyl chain. The peak 1041 $\mathrm{cm^{-1}}$ that appears in PVC-P comes from the C–O vibrations from the DINP plasticizer. For the PVC-R sample, a minor peak located at 1069 $\mathrm{cm^{-1}}$ is recorded. Its presence can be related to the C–O vibration from the solvent residues in the polymer matrix. A sharp peak that appears at 1123 $\mathrm{cm^{-1}}$ in the PVC-P sample can be ascribed to the C–O–C vibration from the DINP plasticizer, while the peaks at 1202 $\mathrm{cm^{-1}}$ possibly come from C–C and/or C–O vibrations. The following peaks at 1256 $\mathrm{cm^{-1}}$ and 1273 $\mathrm{cm^{-1}}$ can be related to the C–O stretching and C–N stretching, respectively. Next, 1424 $\mathrm{cm^{-1}}$ and 1461 $\mathrm{cm^{-1}}$ can also be related to the –C–H bending vibrations, while the peaks located at 1578 $\mathrm{cm^{-1}}$ and 1593 $\mathrm{cm^{-1}}$ that are seen in the PVC-P sample are characteristic of the C=C stretching in the aromatic ring from the DINP plasticizer, likewise, the peak at 1720 $\mathrm{cm^{-1}}$ comes from C=O vibration in DINP. Bands located at 2849 $\mathrm{cm^{-1}}$ and 2917 $\mathrm{cm^{-1}}$ are characteristic of the symmetric and asymmetric vibrations of CH_2 group, while bands at 2870 $\mathrm{cm^{-1}}$ and 2956 $\mathrm{cm^{-1}}$ can be ascribed to symmetric and asymmetric vibrations in CH_3

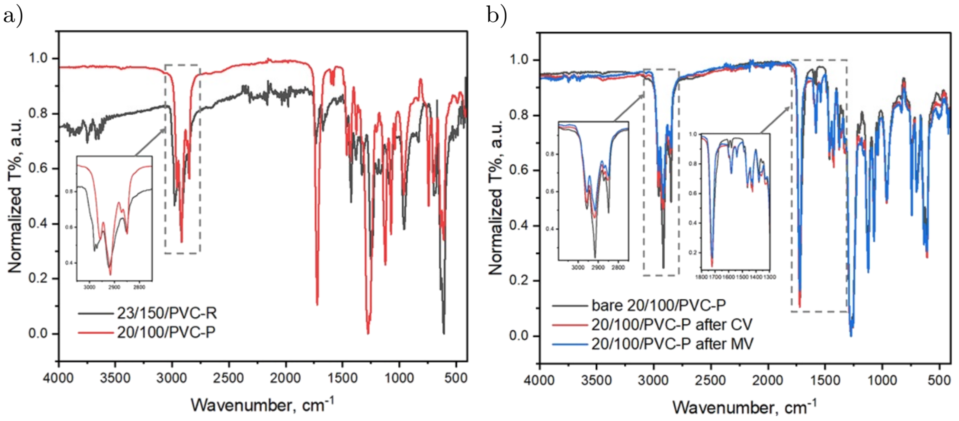

Fig. 4. Normalized FTIR spectra of a) bare 23/150/PVC-R and 20/100/PVC-P, and b) 20/100/PVC-P before and after CV and MV treatment.

functional groups in the alkyl chain [29]. The different intensities, as well as the number of bands, come from the compositional differences related to the plasticizer presence in the PVP-P sample. The spectra of PVC-P before and after CV and MV treatment, that are presented in Fig. 4b, confirm the dyes' adsorption onto the adsorbent through the appearance of a band located at 1539 cm^{-1} that relates to the N–H vibration in the dye molecules adsorbed onto the membranes, as well as through the different ratio between $-\mathrm{CH}_2$ and $-\mathrm{CH}_3$-related bands in the 2800–3000 cm^{-1} region. Additionally, the shift of the band at 1202 cm^{-1} toward lower wavenumbers and a shift of the bands at 1164 cm^{-1} are in the region for C–O–C and/or C–N vibrations. The changes in the spectra after dyes' adsorption come from the intermolecular interactions between the membrane and dyes through the electrostatic interactions, hydrogen bonds, van der Waals, and/or π–π interactions (rings in the dye and plasticizer).

As the wastewater can have a different pH, its influence on the $H\%$ was evaluated, where the contact time of about 550 min was chosen. Adsorption studies performed in solutions of different pH show that 20/100/PVC-P is an effective adsorbent. Due to this, the effectiveness increased to ~80 % for CV, and to ~55 % for MV, at the same pH value, respectively (Fig. 5a). The amount of remain-

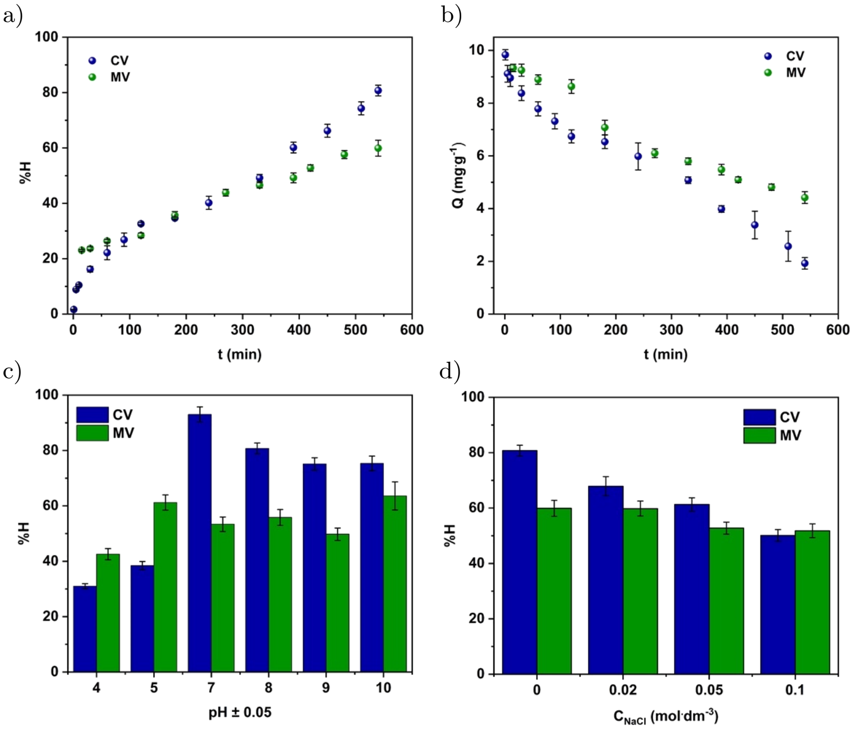

Fig. 5. Adsorption effectiveness of CV and MV of 20/100/PVC-P: a) as a function of time at pH 8.0, b) change the dye concentration as a function of time, c) in various pH ranges, d) in relationship to the varying ionic strength.

ing dyes after the process was ~1.5 mg·g^{-1} for CV, and 4.3 mg·g^{-1} for MV (Fig. 5b). However, the highest effectiveness was recorded for pH 7.0 for CV and 10.0 for MV. It is associated with the negative charge of the membrane at those pH values (Fig. 5). Nevertheless, with the increasing salinity of the solutions, the effectiveness of the adsorption process decreases of about ~5 % for MV, and 30 % for CV, respectively (Fig. 5d). For comparison, commercial polymeric membranes such as PVDF, PAN, or PES typically achieve cationic dye removal efficiencies of 60 % to 90 % depending on surface modification [30–34]. The adsorption performance of the PVC-P membrane (80 % for CV and 55 % for MV) is therefore comparable to or only slightly lower than that of modified commercial membranes, confirming its potential as a cost-effective and sustainable alternative derived from recycled waste.

The kinetic study of 20/100/PVC-P material was investigated at pH equal to 8.0 and 7.0, where the highest CV and MV removal effectiveness was measured, using linear equations (3) and (4) for:

- pseudo-first-linear order:

$$\log\left(Q_e - Q_t\right) = \log Q_e - \left(\frac{k_1}{2.303}\right) t, \tag{3}$$

- pseudo-second-linear order:

$$\frac{t}{Q_t} = \frac{1}{k_2} Q_e^2 + \frac{t}{Q_e}, \tag{4}$$

where Q_e – amount of adsorbate at equilibrium; Q_t – amount of adsorbate at time t; k_1 and k_2 – adsorption rate constants for the pseudo-first-order and pseudo-second-order kinetic models, respectively.

Based on the correlation coefficient (R^2) the adsorption process for the data presented in Fig. 6 for both dyes in both pH conditions undergoes pseudo-first-order kinetics. Importantly, as the amount of adsorbent from the calculations corresponds to the amount of adsorbent from the experimental data, it means that both substances achieved an equilibrium state. Table 2 shows a set of parameters for different kinetic models.

The adsorption of CV and MV onto 20/100/PVC-P is based on the physical interactions, where adsorption is faster at the initial stage for the access to many active sites on the surface of the membrane. Then, it slows down as active sites get filled with adsorbed molecules as long as the adsorbent reaches equilibrium, where the active sites are no longer available. As the studies confirm only weak interactions between the membrane and dye-based model pollutants, the adsorbent can be reused; however, the desorption of the dyes should be optimized.

Membranes made of bare PVC are not commonly reported in the literature for the removal of different types of organic dyes. Literature shows mainly

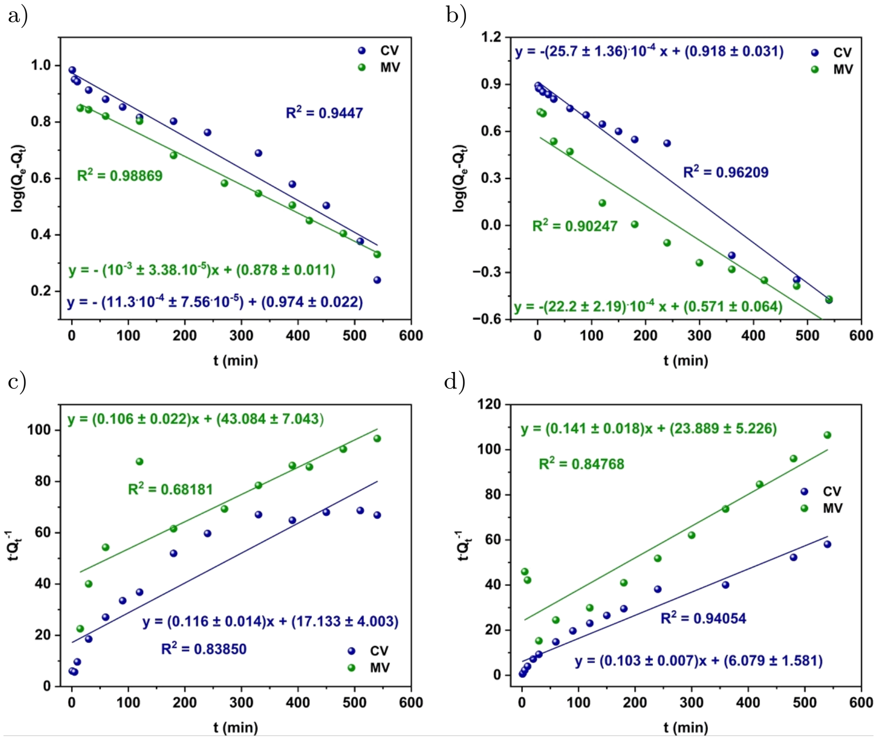

Fig. 6. Linear kinetics order at various pH values for 23/150/PVC-P sample: a) I kinetic order at pH equal 8.0, b) I kinetic order at pH equal 7.0, c) II kinetic order at pH equal 8.0, d) II kinetic order at pH equal 7.0.

Table 2. Parameters of fitting kinetics order for PVC-P at different pH values.

Dye	pH range	Kinetic order	Q_{exp} $[\mathrm{mg}\cdot\mathrm{g}^{-1}]$	Q_{cal} $[\mathrm{mg}\cdot\mathrm{g}^{-1}]$	k	R^2
CV	pH 8.0	pseudo-first	9.812 ±0.343	9.419 ±0.174	$2.602\cdot10^{-3}$ $\pm1.742\cdot10^{-4}$ min^{-1}	0.9447
MV			7.724 ±0.309	7.554 ±0.078	$2.303\cdot10^{-3}$ $\pm7.803\cdot10^{-5}$ min^{-1}	0.98869
CV		pseudo-second	9.812 ±0.343	8.584 ±0.071	4.301 ±0.184 $\mathrm{g}\cdot\mathrm{mg}^{-1}\cdot\mathrm{min}^{-1}$	0.83850
MV			7.724 ±0.309	9.412 ±0.045	2.057 ±0.126 $\mathrm{g}\cdot\mathrm{mg}^{-1}\cdot\mathrm{min}^{-1}$	0.68181
CV	pH 7.0	pseudo-first	9.637 ±0.385	8.276 ±0.031	$5.919\cdot10^{-3}$ $\pm3.137\cdot10^{-4}$ min^{-1}	0.98869
MV			5.409 ±0.135	3.724 ±0.504	$5.113\cdot10^{-3}$ $\pm5.042\cdot10^{-4}$ min^{-1}	0.90247
CV		pseudo-second	9.637 ±0.385	9.741 ±0.145	8.287 ±0.057 $\mathrm{g}\cdot\mathrm{mg}^{-1}\cdot\mathrm{min}^{-1}$	0.94054
MV			5.409 ±0.135	7.097 ±0.056	3.972 ±0.009 $\mathrm{g}\cdot\mathrm{mg}^{-1}\cdot\mathrm{min}^{-1}$	0.84768

PVC-based composites to be used for membrane fabrication. Agaguena *et al.* [35] reported the adsorption of methylene blue by a membrane composed of PVC/PVC-based copolymer with PDMAEM(N+) reaching 87.23 % adsorption efficiency of methylene blue. However, for crystal violet, the $H\%$ was only about

1.66 % at pH 7.0, and the process followed a pseudo-second-order kinetic model [35]. Landarani *et al.* [36] presented an iron(III)–polyvinyl chloride (PVC)–Schiff base adsorbent for the removal of methyl orange, achieving nearly 90 % removal at a dye concentration of 20 ppm at pH 7.0, following a pseudo-second-order kinetic model. The $H\%$ values presented in this work are much higher than those that are mentioned in the literature for differing materials. The effect relates to the different composition and morphology of the membranes resulting in different interactions between the dyes and a surface of the membrane.

4. Conclusions

Recycling of poly(vinyl chloride) is hindered due to low thermal stability of the polymer as well as the use of various organic and mineral additives during its processing. In this work, we present a simple method for reusing PVC waste, based on its dissolution in an organic solvent followed by electrospinning, to prepare a textile-like membrane made of fibers for water purification. To obtain the membrane with desired physicochemical characteristics, unplasticized PVC and PVC containing DINP plasticizer were used. The SEM images revealed differences in the plasticized and unplasticized electrospun fiber-based membranes, where PVC-P offered a quite tight fibrous structure compared to the PVC-R material. Contact angle studies revealed much better wetting of the PVC-P material over the PVC-R, which correlated with the adsorption studies using cationic dyes like CV and MV. Those dyes were removed from the aqueous solutions with the highest effectiveness above $\mathrm{pH}_{\mathrm{ZPC}}$ values in slightly alkali media. Kinetic studies show the possibility of reusing the membrane by implementing the desorption of dyes. The results demonstrated that PVC waste can be successfully utilized in electrospinning, and the obtained fibrous membranes show great potential for the application in water treatment processes, e.g., for industrial purposes.

Acknowledgements

This work was supported by the Miniatura grant financed from the National Science Centre (NCN) under the grant number: DEC-2024/08/X/ST11/00498 and the National Science Foundation under the grant program International Research Experience for Students (NSF IRES 21072201 SOLARIS).

References

1. Lewandowski K., Skórczewska K., A brief review of poly(vinyl chloride) (PVC) recycling, *Polymers*, **14**: 3035, 2022, https://doi.org/10.3390/polym14153035.
2. Xu Z., Kolapkar S.S., Zinchik S., Bar-Ziv E., McDonald A.G., Comprehensive kinetic study of thermal degradation of polyvinylchloride (PVC), *Polymer Degradation*

and Stability, **176**: 109148, 2020, https://doi.org/10.1016/j.polymdegradstab.2020.109148.

3. Liu L., Yan B., Liu T., Zhang Y., Du R., Wang J., Chen G., Cheng Z., Chemical recycling of polyvinyl chloride: Recent progress in pretreatment dechlorination and chlorine recycling, *Resources, Conservation and Recycling*, **222**: 108471, 2025, https://doi.org/10.1016/j.resconrec.2025.108471.
4. Wagner S., Schlummer M., Application of solvent-based dissolution for the recycling of polyvinylchloride flooring waste containing restricted phthalate plasticizers, *Resources, Conservation and Recycling*, **211**: 107889, 2024, https://doi.org/10.1016/j.resconrec.2024.107889.
5. Skórczewska K., Szulc J., Lewandowski K., Ligocka A., Wilczewski S., Modification of poly(vinyl chloride) with bio-based cassia oil to improve thermo-mechanical and antimicrobial properties, *Materials*, **16**: 2698, 2023, https://doi.org/10.3390/ma16072698.
6. Youness F., Akhtiyar S., Tehrani-Bagha A., Bilbeisi R.A., Progress in modified electrospun PVC membranes: Toward sustainable solutions for environmental remediation, *Separation and Purification Technology*, **359**: 130456, 2025, https://doi.org/10.1016/j.seppur.2024.130456.
7. Bonakdar M.A., Rodrigue D., Electrospinning: Processes, structures, and materials, *Macromol*, **4**(1): 58–103, 2024, https://doi.org/10.3390/macromol4010004.
8. Stramarkou M., Tzegiannakis I., Christoforidi E., Krokida M., Use of electrospinning for sustainable production of nanofibers: A comparative assessment of smart textiles-related applications, *Polymers*, **16**(4): 514, 2024, https://doi.org/10.3390/polym16040514.
9. Escriba Flores A.A., Sanches de Almeida D., Lopes Aguiar M., Cava C.E., Enhanced air filtration efficiency through electrospun PVC/PVP/MWCNTs nanofibers: Design, optimization, and performance evaluation, *ACS Omega*, **9**(36): 37771–37779, 2024, https://doi.org/10.1021/acsomega.4c03628.
10. Zulfi A., Hartati S., Nur'aini S., Noviyanto A., Nasir M., Electrospun nanofibers from waste polyvinyl chloride loaded silver and titanium dioxide for water treatment applications, *ACS Omega*, **8**(26): 23622–23632, 2023, https://doi.org/10.1021/acsomega.3c01632.
11. Wang Z., Kang S.B., Yang E., Won S.W., Preparation of adsorptive polyethyleneimine/polyvinyl chloride electrospun nanofiber membrane: Characterization and application, *Journal of Environmental Management*, **316**: 115155, 2022, https://doi.org/10.1016/j.jenvman.2022.115155.
12. Amalia R., Noviyanto A., Rahma L.A., Merita, Labanni A., Fahroji M., Purwajanti S., Hapidin D.A., Zulfi A., PVC waste-derived nanofiber: Simple fabrication with high potential performance for PM removal in air filtration, *Sustainable Materials and Technologies*, **40**: e00928, 2024, https://doi.org/10.1016/j.susmat.2024.e00928.

13. Mani S., Bharagava R.N., Exposure to Crystal Violet, Its Toxic, Genotoxic and carcinogenic effects on environment and its degradation and detoxification for environmental safety, in: de Voogt W. (ed.), *Reviews of Environmental Contamination and Toxicology*, Vol. 237, pp. 71–104, Springer, Cham, 2016, https://doi.org/10.1007/978-3-319-23573-8_4.

14. Kua T.L., Kooh M.R.R., Dahri M.K., Zaidi N.A.H.M., Lu Y.C., Lim L.B.L., Aquatic plant, Ipomoea aquatica, as a potential low-cost adsorbent for the effective removal of toxic methyl violet 2B dye, *Applied Water Science*, **10**: 243, 2020, https://doi.org/10.1007/s13201-020-01326-9.

15. Chi Z., Liu R., Zhao X., Sun Y., Yang B., Gao C., Study on the genotoxic interaction of methyl violet with calf thymus DNA, *Applied Spectroscopy*, **63**(12): 1331–1335, 2009, https://doi.org/10.1366/000370209790109085.

16. Cruz P.P.R., da Silva L.C., Fiuza-Jr R.A., Polli H., Thermal dehydrochlorination of pure PVC polymer: Part I – thermal degradation kinetics by thermogravimetric analysis, *Journal of Applied Polymer Science*, **138**: e50598, 2021, https://doi.org/10.1002/app.50598.

17. Nishibata H., Uddin Md.A., Kato Y., Simultaneous degradation and dechlorination of poly (vinyl chloride) by a combination of superheated steam and CaO catalyst/adsorbent, *Polymer Degradation and Stability*, **179**: 109225, 2020, https://doi.org/10.1016/j.polymdegradstab.2020.109225.

18. Briesemeister M., Gómez-Sánchez J.A., Bertemes-Filho P., Pezzin S.H., PVC/CNT electrospun composites: Morphology and thermal and impedance behavior, *Polymers*, **16**(20): 2867, 2024, https://doi.org/10.3390/polym16202867.

19. Zhao J., Ma H., Huang H., Zhang J., Chen Y., Experimental investigation and numerical modeling of oxidative pyrolysis mechanism of mining PVC cable sheath, *Journal of Thermal Analysis and Calorimetry*, **147**: 14479–14490, 2022, https://doi.org/10.1007/s10973-022-11723-8.

20. Lu Yh., Chen Zl., Lu Yw., Synthesis, characterization and thermal behavior of plasticized poly (vinyl chloride) doped with folic acid-modified titanium dioxide, *Scientific Reports*, **12**: 3379, 2022, https://doi.org/10.1038/s41598-022-07177-5.

21. Gartili A., Caillol S., Briou B., Lapinte V., One step beyond for CNSL-based plasticizers for PVC: Use of cardol, *European Journal of Lipid Science & Technology*, **126**: e2400086, 2024, https://doi.org/10.1002/ejlt.202400086.

22. Pham Le Q., Uspenskaya M.V., Olekhnovich R.O., Baranov M.A., The mechanical properties of PVC nanofiber mats obtained by electrospinning, *Fibers*, **9**(1): 2, 2021, https://doi.org/10.3390/fib9010002.

23. Boraei S.B.A., Bakhshandeh B., Mohammadzadeh F., Haghighi D.M., Mohammadpour Z., Clay-reinforced PVC composites and nanocomposites, *Heliyon*, **10**: e29196, 2024, https://doi.org/10.1016/j.heliyon.2024.e29196.

24. Lenzi L., Esposti, M.D., Braccini S., Siracusa C., Quartinello F., Guebitz G.M., Puppi D., Morselli D, Fabbri P., Further step in the transition from conventional

plasticizers to versatile bioplasticizers obtained by the valorization of levulinic acid and glycerol, *ACS Sustainable Chemistry & Engineering*, **11(**25): 9455–9469, 2023, https://doi.org/10.1021/acssuschemeng.3c01536.

25. Quoc Pham L., Uspenskaya M.V., Olekhnovich R.O., Olvera Bernal R.A., A review on electrospun PVC nanofibers: fabrication, properties, and application, *Fibers*, **9**(2): 12, 2021, https://doi.org/10.3390/fib9020012.
26. Zhong Y., Wang K., Guo C., Kou Y., Hassan A., Lu Y., Wang J., Wang W., Competition adsorption of malachite green and rhodamine B on polyethylene and polyvinyl chloride microplastics in aqueous environment, *Water Science & Technology*, **86**(5): 894–908, 2022, https://doi.org/10.2166/wst.2022.252.
27. Jang M.H., Kim M.S., Han M., Kwak D.H., Experimental application of a zero-point charge based on pH as a simple indicator of microplastic particle aggregation, *Chemosphere*, **299**: 134388, 2022, https://doi.org/10.1016/j.chemosphere.2022.134388.
28. Pietrzyk P., Borowska E.I., Hejduk P., Camargo B.C., Warczak M., Nguyen P.T., Pregowska A., Gniadek M., Szczytko J., Wilczewski S., Osial M., Green composites based on volcanic red algae *Cyanidiales,* cellulose, and coffee waste biomass modified with magnetic nanoparticles for the removal of methylene blue, *Environmental Science and Pollution Research*, **30**: 62689–62703, 2023, https://doi.org/10.1007/s11356-023-26425-3.
29. Smith B.C., The infrared spectra of polymers III: Hydrocarbon polymers, *Spectroscopy*, **36**(11): 22–25, 2021, https://doi.org/10.56530/spectroscopy.mh7872q7.
30. Zhao J, Liu H., Xue P., Tian S., Sun S., Highly-efficient PVDF adsorptive membrane filtration based on chitosan@CNTs-COOH simultaneous removal of anionic and cationic dyes, *Carbohydrate Polymers*, **274**(15): 118664, 2021, https://doi.org/10.1016/j.carbpol.2021.118664.
31. Sultana S., Chakraborty D., Parvez D.A., Chandan M.R., Rahaman M., Polymeric membranes for advanced separation and sensing: Materials and mechanisms for emerging applications – A review, *Chemistry an Asian Journal*, **28**(18): e00714, 2025, https://doi.org/10.1002/asia.202500714.
32. Elnagar E.R., Hamdy G., Abdallah H., Ali S.S., Taher F.A., Enhanced performance of polyvinylidene fluoride with triethanolamine and polyethylene glycol ultrafiltration membrane for textile wastewater treatment, *International Journal of Environmental Science and Technology*, **22**: 5529–5542, 2025, https://doi.org/10.1007/s13762-024-05938-5.
33. Rianjanu A., Recent advances in electrospun nanofiber membranes for dye filtration: A focused mini-review, *Environmental Chemistry and Safety*, **1**(2): 9600018, https://doi.org/10.26599/ECS.2025.9600018.
34. Khan I.A., Khan A.U., Butt M.S., Janjua A., Uddin E., Deen K.M., Sadiq R., Ahmad N.M., Dye removal from contaminated water through PES membranes enhanced with the incorporation of switchable polyacrylic acid grafted on graphene

oxide, *ACS Omega*, **10**(26): 28178–28190, 2025, https://doi.org/10.1021/acsomega.5c02815.

35. Agaguena A., Benbellat N., Khaoua O., Bendaikha T., Kinetic adsorption of methyl blue dye from aqueous solution by PVC/PVC-based copolymer containing quaternary amine, *Analytical Science*, **39**: 1371–1383, 2023, https://doi.org/10.1007/s44211-023-00356-y.
36. Landarani M., Arab Chamjangali M., Bahramian B., Preparation and characterization of a novel chemically modified PVC adsorbent for methyl orange removal: Optimization, and study of isotherm, kinetics, and thermodynamics of adsorption process, *Water, Air & Soil Pollution*, **231**: 513, 2020, https://doi.org/10.1007/s11270-020-04874-7.

2. Application of Power Ultrasound Treatment in the Preparation of Cement-Based Composites

Paweł Lisowski

Institute of Fundamental Technological Research, Polish Academy of Sciences
Warsaw, Poland
e-mail: plisowsk@ippt.pan.pl

In order to enhance cementitious material hydration and increase the efficacy of substituting supplemental cementitious materials (SCMs) in terms of physicochemical and mechanical properties, a new approach such as the power ultrasound treatment (PUS) is presently being considered. The process by which PUS acts in cement-based composites is poorly understood, and a handful of studies have looked into this promising field. This is an up-to-date study that compiles all the information available for cement-based composites design and development, taking into account all PUS phenomena. Additionally, prior research on the mechanical and physicochemical effectiveness of PUS on cement pastes, mortars, and supplementary cementitious materials is reviewed and analyzed. This study also examines possible future directions, such as combining PUS with other physical processes like sonofragmenation to further improve treatment efficiency during PUS treatment. The conclusion of this study offers some remarks and future research perspectives that are required to obtain a fundamental understanding of this new field related to PUS treatment.

Keywords: power ultrasound treatment, early strength development, Portland cement, sonofragmentation, cement-based composites.

https://doi.org/10.24423/9788365550682.ch2

Abbreviations

ASZ – amorphous synthetic zeolite,
DSF – densified silica fume,
GO – graphene oxide,
GBFS – granulated blast furnace slag,

MK	metakaolin,
NS	nano-silica,
PCS	polycarboxylate superplasticizer,
PC	Portland cement,
PUS	power ultrasound treatment,
SF	silica fume,
SP	superplasticizer,
SCMs	supplementary cementitious materials.

1. Introduction

The Portland cement's (PC) hydration process, which entails the conversion of anhydrous to hydrate phases, is generally acknowledged to be a complex dissolution-precipitation process [1]. Cement hydration products are characterized by a combination of interdependent microstructural and chemical phenomena and kinetic mechanisms of PC hydration, which are not fully understood. However, considerable effort has been invested in enhancing the perceived performance of PC in cement-based composites through an environmentally sustainable approach [1]. The idea of replacing PC with supplementary cementitious materials (SCMs) has recently generated a lot of scientific and environmental discussion to mitigate the use of natural resources and CO_2 emissions during cement production. The inferior early strength performance of low-CO_2 cement-based composites is the major reason impeding their use in practice [2, 3].

Improved consistency and fresh cement-based composite properties [4], reduced hydration heat evolution [5], enhanced mechanical/structural properties such as long-term strength development [6], increased durability [7–9], and decreased autogenous shrinkage [10] are some of the advantages that have been studied in cement-based materials that incorporate SCMs. Nevertheless, the application of SCMs frequently results in increased drying shrinkage [10, 12], decreased early strength development [6], prolonged setting times [11], reduced freeze-thaw resistance [13–15], decreased scaling resistance [13–15], and decreased slump flow and workability [13–15].

To maintain production cycles, high early strength is vital for the application of concrete technologies in modern construction. This issue can be resolved by using heat treatment, hardening accelerators, or cement clinker that contains more reactive strength-determining ingredients (like alite) [2, 3, 13–15]. Three primary approaches have been investigated to address the limitations and enhance the effectiveness of PC and SCMs in cementitious systems: thermal, mechanical, and chemical. There are two types of heat treatment, or thermal activation: calcination [16–18] and increased temperature curing [19]. Chemical activators [20, 21] can be used to chemically modify PC and SCMs, which can immediately disintegrate the structure, fracture the chemical bonds, and promote the formation of cement-based composites. The reactivity of the amorphous phases, the reduction of the specific surface area and soluble fraction, and the increase in the crystalline fraction have all been found to be limiting factors for the former. In cementitious materials that incorporate SCMs at later ages, the latter frequently results in reduced strength development [22, 23]. By grinding certain types of SCMs into ultrafine powders over an extended period, mechanical methods have been widely used to enhance their pozzolanic activity. This accelerates the pozzolanic reaction rate and, in turn, the strength development of cement-based composites containing SCMs by decreasing the particle size distribution and increasing the dissolution of pozzolans [13–15].

Recently, power ultrasound (PUS) treatment has been developed as an unconventional method to improve the mechanical and microstructural properties of cement-based composites. In materials science and engineering, PUS has been applied to a variety of processes, including particle dispersion, surface cleaning, degassing, and nanostructure production. While some of these applications have been thoroughly studied, others, like the use of PUS to improve the properties of SCMs containing composites and regulate the performance and properties of cementitious materials, have not yet been examined and provide interesting new opportunities. In order to provide an overall assessment of the mechanical strength, porosity, permeability, and durability of cementitious composites, a number of PUS techniques have been employed to characterize the hardening and setting processes of cement pastes, mortar, and concrete. The impact of PUS on the efficiency of cementitious matrices and composites' early age hydration reactions, including SCMs, has been investigated in a few studies [24, 25].

The literature on PUS's impact on SCMs and cement-based composite preparation is examined in this work, along with some of the underlying mechanisms in action. We compare the effects of various PUS power and time on compressive strength. Additionally, this work aims to help disperse SCMs and cement paste by using the PUS technology. The most advantageous ultrasonic parameters for cement-based material strength development are identified using this method. PUS's potential uses in cement-based materials will also be taken into account.

2. Basic principles of the role of PUS in the preparation of cement-based composites

Sound waves with a frequency higher than the human auditory limit (often ≥20 kHz) are referred to as ultrasound. Physical and chemical processes are involved in PUS. The mechanical impact of unstable cavitation prevails at low frequencies (20 kHz to 80 kHz), and the bubbles collapse more violently as the frequency gets closer to 20 kHz [24, 26]. The chemical impact is stronger at high frequencies (>100 kHz), when more bubbles develop and collapse with less force. Regarding the PUS's chemical impacts, the precise term 'sonochemistry' was specifically created to refer to a unique field of research where strong PUS either initiates chemical reactions or just takes part in some chemical processes as the potentially disruptive and unconventional technology. Sonochemistry's versatility across a wide range of domains can be attributed to its widespread application. Furthermore, the 'cavitation' effect – that is, the continuous rarefaction and compression cycles – occurs when an ultrasonic wave passes via a liquid medium, and is responsible for the most often seen effects of PUS treatment on solid surfaces and chemical reactions. Acoustic cavitation or implosion is the term used to describe this bubble formation, growth and an implosion process. Extreme temperatures (5000 K) and pressures (1000 bar) generated by cavitation bubbles (Fig. 1) have the potential to produce extremely high shear forces [24–26]. High-speed jets, reactive radicals, and shock waves all accompany this spectacular collapse at the same time. These extreme conditions are the main preconditions for the special physico-chemical processes that sonic cavitation in liquids causes. The heart of sonochemistry is the PUS irradiation of liquids, which locally creates pressure changes to support green chemistry's objectives by employing more environmentally friendly techniques to address the current environmental challenges. PUS treatment can solve problems with cement particle hydration, such as hydration rate control, packing density control, and aggregation/agglomeration, when preparing cement-based composites. The mechanical properties and durability of hardened cement materials are greatly influenced by pore structure, and hydration mechanisms during PUS treatment are intricate [24–27]. The early age and long-term strength properties of cement-based composites are largely controlled by the penetration/dissolution of anhydrous phases during hydration [24–27]. PUS does not affect the overall heat release, but it speeds up the heat release rate during the hydration acceleration phase [25] (Fig. 2). Rapid cement hydration is probably the cause of the increased strength growth in PUS treatment of cement suspensions that is seen for the first 16 h [25].

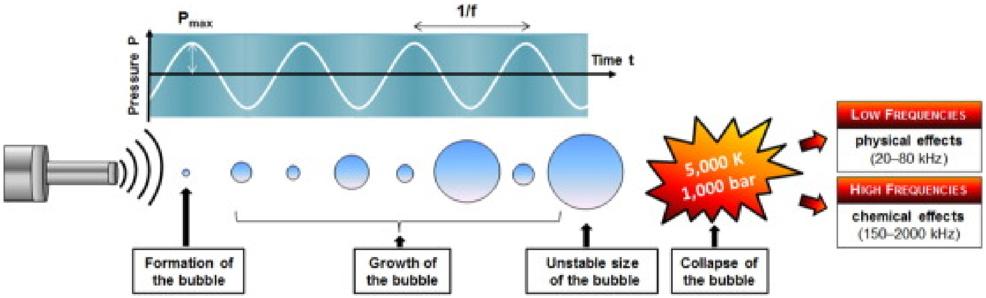

Fig. 1. PUS methodology (open access status) [25].

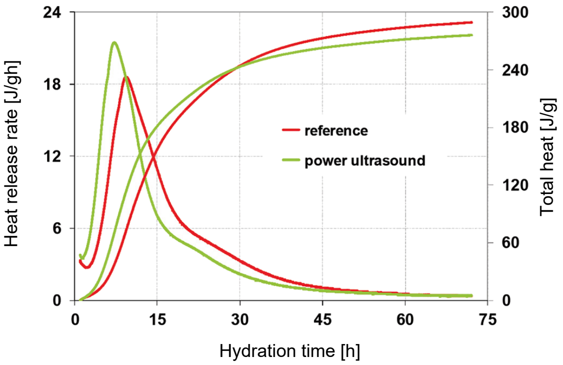

Fig. 2. PUS treatment's impact on cement hydration (open access status) [25].

It is noteworthy that PUS can achieve a high dispersion of particles uniformly dispersed into cement paste, increase the specific surface area, improve the pozzolanic reactivity of mineral additives, change the degree of de-agglomeration (particles become more stable and have a lower propensity to agglomerate), and alter the particle size distribution in favour of smaller particle sizes. Furthermore, during the cement hydration-acceleration phase, PUS can accelerate the heat release rate.

3. Supplementary cementitious materials treated by PUS

There are several methods for avoiding agglomerates, including mixing and grinding. Deagglomeration is physically limited by both of these techniques, and because the particles come into close contact with the mill, contaminants may be added. However, PUS treatment can offer many options for reducing agglomeration in liquid suspensions of particles (Table 1). Additionally, it has

Table 1. Supplementary cementitious materials treated by PUS.

Material subjected to sonication	Power of PUS [W]	Frequency of PUS [kHz]	Treatment time [min]	Ref.
Densified silica fume	600	20	2–20	[28]
Silica fume	215	35	5–35	[29]
	30	20	0.25–60	[30]
	750	20	10	[31]
Nano silica	400	24	10	[32]
	135	59	5	[33]
Metakaolin	720	20	60	[34]
Zeolite	60	28	15	[35]
Electric arc furnace slag	120	40	30	[36]

been used extensively to disperse mineral additives in aqueous solution based on acoustic cavitation caused by PUS treatment, such as silica fume [29, 37], clays [38], and glass fume [39].

PUS dispersion has the important advantage of producing silica fume (SF) particles that are usually 1 μm or smaller, which raises the reactivity of SF in concrete [40]. An ultrasonic dispersion device is installed in the water tank as part of the industrial concrete manufacturing process to incorporate ultrasonic dispersion. In order to create a suspension, the necessary quantity of SF is added first. The apparatus for dispersing ultrasonic waves is then turned on before the suspension is added to the concrete mix while it is being mixed [40]. According to Fraga *et al.* [31], sonication effectively disperses silica fume, increasing the amount of C-S-H phase and densifying cement pastes' microstructure that includes SF. When densified SF was subjected to a 25 min of PUS treatment, the particle size decreased from 22 μm to 4 μm [28]. Similar outcomes to those of Wang *et al.* [41] were obtained using the ultrasonic dispersion technique. After 12 min of PUS treatment, the low-grade silica fume's particle size was less than 10 μm, while the high-grade silica fume's was around 4 μm [41]. Additionally, the de-agglomeration of particle agglomeration by PUS treatment is a key step in the sonication process. Therefore, 12 min can serve as a useful reference point for analysing how the sonication dispersion duration affects the distribution of SF particles [41]. According to Ni *et al.* [42], the densified silica fume (DSF) particles clearly raise the cement's hydration heat release rate considerably following ultrasonic treatment. Martınez-Velandia *et al.* [28] investigated the sonication procedure of the DSF to deagglomerate the SF and reduce particle sizes. Sonication improved the pozzolanic properties of DSF and increased the pace of interaction with calcium hydroxide by producing a larger proportion of extremely small particles. Additionally, this behaviour makes it possible to increase the mechanical strength of mortars prepared with sonicated silica fume. Submicrometric particles might be produced in greater quantities by increasing the sonication power level and duration. According to Rodríguez *et al.* [43], densified silica fume's reactivity is increased by sonication through the deagglomeration process. When SF particles were evenly distributed throughout the cement paste, the C-S-H phase development was accelerated. Cement pastes prepared with the sonicated SF showed a significant reduction in calcium hydroxide concentration after 28 days of curing. In contrast to samples prepared with raw silica fume, Wang *et al.* [44] found that cement paste that had solidified and included sonication-treated SF had higher strength, indicating more efficient dispersion of sonication-treated SF in the cementitious materials. The pozzolanic activity of SF in cementitious materials was enhanced to generate calcium silicate hydrate, which improved the compressive strength. This was due to the silica fume's good particle size distribution and improved cementitious material dispersion [45].

The use of dispersion techniques prior to mixing and in conjunction with high-shear mixing, such as silica fume-slurry preparation using sonication treatment [46], can serve as an alternative method of preparation for paste samples. Agglomerates frequently undergo partial disintegration after PUS treatment, resulting in tiny fragmented agglomerates that are usually around 0.5 μm in size. However, the degree of partial fragmentation breakdown varies greatly throughout densified silica fumes. Relatively short ultrasonic treatments are typically used for dispersion treatments, which separate individual particles from one another [46]. The moderate PUS treatment can disperse DSF from some sources into tiny chains of spheres or clusters, whereas other sources resist this treatment and mostly stay as massive agglomerates. Large amounts of agglomerates are nearly always retained in concrete under standard mixing conditions. The undispersed agglomerates that remain in concrete following mixing frequently have sizes larger than the PC particles, which limits the potential advantages of the fine particle filler effect [47].

Concrete's microstructure can be strengthened and consolidated by adding nano-silica (NS), which introduces nucleation sites for the precipitation and growth of hydrate phases at the nanoscale. In addition to reducing concrete shrinkage through its seeding action, appropriately sonicated NS may have increased the effect of NS on concrete by delaying the agglomeration of particles [32]. The most important de-agglomeration technique was sonication, which increased the concrete's compressive strength by 23 % with just 1 % nano silica (NS) substituted for cement [33]. Because NS is more dispersed after sonication, concrete workability was also much increased. The results showed that adding a modest quantity of NS shortens the setting time and increases the compressive strength after 3 and 7 days. When it comes to properly dispersing nano-silica, PUS treatment of the combination with water is likely a better option than mechanical mixing [48]. Hydrothermal synthesis can potentially be substituted with the sonication process. A method for turning rice husk ash into belite cement is described by Rodrigues [49]. In contrast to earlier studies, sonication, which is as effective but far less costly, replaced the hydrothermal treatment [49].

The scalable and environmentally friendly ultrasonic method that Long *et al.* [34] devised for the efficient preparation of high-dispersity metakaolin (MK) also shows a notable increase in cement composites' compressive strength. These findings would allow MK to be used in cement composites more successfully by increasing their advantages and reducing their cost. Carbon nanotubes must be uniformly dispersed, and this is accomplished by using a sonication approach [50]. Sonicating PC and carbon nanotubes at the same time is another technique for dispersing carbon nanotubes [51, 52]. After 3 days of hardening, sonication of the cement paste, irrespective of the presence of amorphous synthetic zeolite, considerably improves the compressive strength [35]. The aragonite whiskers, which fill the cement paste's pores as nanomaterials, can be evenly distributed by PUS. Furthermore, the nucleation of C-S-H during hydration was aided by the exposed silica-rich surface [36]. According to Kawashima *et al.* [53], PC and fly ash–cement pastes were used to examine the effects of sonication and blending of the nano-$CaCO_3$ on the hydration rate, setting time, and early compressive strength growth. In these instances, sonication improved the nano-$CaCO_3$'s impact. Cement composites' mechanical properties have been effectively enhanced by the use of this technique [53].

4. Cement paste and mortars treated by PUS

Given the significant physicochemical impact of PUS, it has considerable promise as a new PUS-assisted mixing technique for making homogeneous cement paste (Table 2). PUS-induced hydration is the primary cause of the mechanical properties. It suggests that cement-based materials may have their mechanical strength increased by the PUS treatment. This could be because sonication improves the material's homogeneity and disrupts the flocculation structure of the cement particles [54, 55, 60].

Table 2. Cement paste under the influence of PUS.

Specimen subjected to sonication	w/c	Power of PUS [W]	Frequency of PUS [kHz]	Treatment time [min]	Ref.
Cement paste	0.50	30–300	20	1–5	[54]
	0.50	593, 541	26, 132	2–10	[56]
	0.35	250	24	10–60	[57]
	0.30 0.50	100, 450, 900	28	1–30	[58]
	0.30 1.00	912	28	3	[59]

PUS can accelerate the early hydration rate, increase the mechanical properties, reduce the cement paste's dynamic yield stress and apparent viscosity, and efficiently disperse flocculated particles, according to a recent study by Xu *et al.* [54]. Following the PUS treatment, the hardened cement paste's C_3S content is marginally lower, and its C_2S level is noticeably lower than that of the cement paste without PUS. A homogenous maximum temperature field can be achieved by using 900 W (28 kHz) PUS treatment for 10 min, according to Xiong *et al.* [58]. PUS increases the compressive strength, accelerates C_3S consumption, and promotes Portlandite formation. The optimal combination of ultrasonic power and irradiation duration is thought to be 900 W for 10 min, taking into account the practical ranges of temperature rise. The acceleration of C_3S hydration by PUS is more noticeable at lower calcium concentrations, according to Remus *et al.* [61]. This implies that cements containing a larger percentage of

SCMs benefit most from the PUS treatment. PUS enhanced the yield of portlandite, precipitated extremely early C-S-H phases and amorphous AH_3, and accelerated the dissolution of Ca^{2+}, Si^{4+} and Al^{3+}, according to recent research by Ehsani *et al.* [62]. Additionally, the effect of PUS treatment on the chemical shrinkage of cement pastes and the development of mortars' compressive and flexural strengths was examined by Ehsani *et al.* [56]. The results demonstrated that applying frequencies of 26 kHz and 132 kHz to the cement paste for 2 min shortly after mixing the rate of chemical shrinkage increased. After mortars were cured for 91 days, sonicating at a more intense acoustic power of 26 kHz led to a faster growth of the compressive and flexural strength. When aggregates were added to the pre-sonicated paste, the flexural strength of mortars increased by 17 % after 28 days, suggesting that the paste-aggregate interface may have changed. PUS-assisted PC mixing was investigated by Xiong *et al.* [63] and applied varying ultrasonic power levels to the cement paste. The results showed that the cement paste's compressive strength, porosity, and degree of hydration all improved. The impact on the paste mixes of a temperature increase brought on by the use of a high-power ultrasonic system was not discussed. Only cement pastes with a w/c ratio of 0.3 were examined.

The impact of the PUS treatment on the pore solution of fresh cement pastes with varying water-to-cement ratios was further investigated by Ehsani *et al.* [64]. Their findings showed that PUS treatment increases the amount of aluminate ions released into the pore solution, which in turn encourages the formation of amorphous aluminum hydroxide hydrate. The PUS treatment is more adaptable and energy-efficient than conventional acceleration methods, like steam curing at high temperatures in the manufacturing of precast concrete. Xiong *et al.* [59] investigated the hydration and dispersion of the cement paste prepared by the PUS-assisted mixing technology. The PUS enhanced strength in the early stages and late hydration ages. After 1 day and 28 days, the compressive strength was increased by 26.1 % and 18.3 %, respectively, compared to the reference specimens. According to these results, PUS-assisted mixing is beneficial for improving the sustainability of building material production.

By applying PUS to fresh PC (frequency: 20 kHz, amplitude: 43 μm, energy input: 75 J/ml), Peters [65] was able to decrease the induction period and increase the heat release during hydration. PUS treatment was shown to primarily accelerate alite hydration without changing the cement's overall reaction pathway. By exposing more unwrapped surfaces of C_3S grains and providing more nucleation sites for the C-S-H growth, the facilitator of mass transfer and the localised erosion effect near the clinker surface significantly increase the precipitation of the very early C-S-H phase, according to the author's theory. Only one PUS power density/frequency was used for the PUS treatment, and a probe-based setup was used for the ultrasonic delivery. In either the cement suspension or the mixed mortar, this resulted in a notable increase in temperature in the high-energy cavitation zone formed near the probe tip. The increased dissolution rate of cement phases may result from erosion and exfoliation of anhydrous grains brought on by the accelerated mass transfer linked to PUS cavitation [24]. Additionally, cavitation can result in degassing or deaeration [66], which removes trapped air and affects the mechanical properties of cement-based composites [24]. In particular, this is true for longer exposure times of PUS treatment.

As high-intensity PUS waves propagate through the cement paste, the most significant energy transfer mechanism is conversion of sound energy into thermal energy [54]. However, there are still several unanswered questions and limitations in the current research on the thermal effect of PUS in the cement paste. In the first place, transducer reactors of the ultrasonic bath or horn types are commonly employed for experimental purposes [67]. Due to the constraints of physical sizes and technical procedures, the sound fields of the two reactors were both heterogeneous, even in the diluted solution [68]. The cement paste's temperature increased significantly near the reactor tips after the PUS treatment with the horn type [65]. The distinctions between the tip position and other positions, however, were not explained in that study. Prior research has not focused on the temperature evolution in the cement paste caused by batch-type reactors. Secondly, it is yet unknown how far the heat effect in cement paste will actually work.

The effects of PUS-assisted preparation on the mechanical and physicochemical properties of cement-granulated blast furnace slag (GBFS) composite pastes are examined for the first time by Lisowski *et al.* [69]. Using PUS in a pulse mode in the vertical jacketed glass sonoreactor with closed-circuit cooling (Fig. 3), specimens with different particle size fractions were obtained. Comparing the best-performing cement-GBFS composite to traditional mixing methods revealed a significant improvement in Vickers hardness and modulus of elasticity (98 % and 74 %,

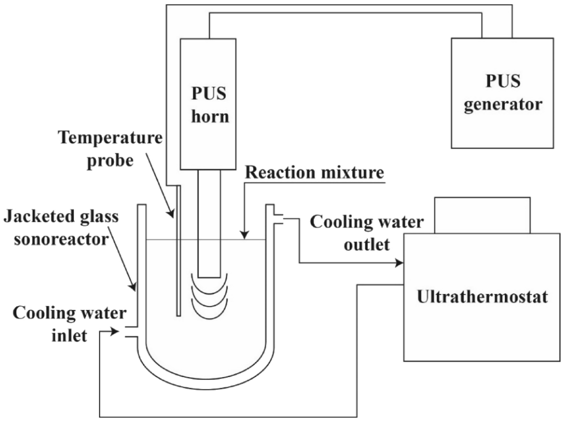

Fig. 3. System for the preparation of cement-GBFS composite under the impact of PUS (open access status) [69].

respectively), as well as compressive and flexural 2-day strengths (132 % and 58 %, respectively). In a similar vein, after 2 days, the BET surface area grew by about 111 %, the cumulative heat release increased by roughly 34 %, and the Portlandite content dropped by roughly 29 %.

The improved PUS treatment, combined with an effective cooling system to regulate the mixture temperatures, makes this study unique when compared to earlier research on PUS in cement systems. This enables progress in identifying the effects of PUS on the hydration and strength development of cement systems containing GBFS. The sonofragmentation (particle size refinement during the PUS treatment) of GBFS particles was tuned to maximize the effectiveness of the PUS treatment (Fig. 4).

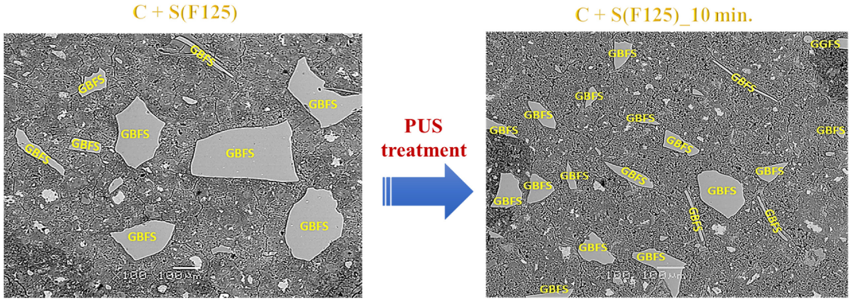

Fig. 4. SEM images of cement-GBFS composite without PUS and under the influence of PUS (open access status) [69].

Another interesting way to increase the early strength of concrete that contains SCMs is the PUS technique. Without sacrificing early strength performance, it is possible to substitute up to 30 % of the cement in concrete with SCMs by using the PUS treatment during the mixing phase [61, 70]. Furthermore, Serelis *et al.* [71] discovered that high-frequency PUS treatment can deagglomerate the SF and microfine cement powder particles. Xiong has also reported similar effects [63]. On the other hand, equally pre-dispersed graphene oxide (GO) was adsorbed on the surface of cement particles and quickly lost its redisperse ability when the cement paste was mixed with the GO aqueous solution [72]. Consequently, PUS is anticipated to enhance the matrix's mechanical properties and microstructure while preserving the graphene oxide's advantageous dispersion state throughout the mixing process. In addition to examining the dispersion and strengthening mechanism of the cement paste modified with GO, Xiong *et al.* [73] suggested the PUS-assisted mixing technique. The modified cement paste's GO particle size was significantly reduced as a result of the PUS-assisted mixing treatment. In cement composites, PUS-assisted mixing is expected to be a viable way to disperse GO and contribute to the realization of nanoengineering's wide-ranging applications.

When the hydrated cement pastes contain polycarboxylate superplasticizer (PCS), Wang *et al.* [57] examined the impact of the PUS treatment on cement hydration. The PUS treatment significantly reduces the setting time and increases the 1-day compressive strength of mortars containing PCS, according to the results, but it does not affect the reference mortar.

PUS's influence on hydration kinetics and deaeration performance by measurement of trapped air in concrete and mortar are two examples of how PUS works in cement-based composites, in spite of the fact that PUS has been used in industry for a variety of purposes [74, 75]. Additionally, bespoke PUS equipment that can perform sonication at different power and frequency levels is also needed. Vaitkevicius *et al.* [76] used a PUS (water-cooled transducer) to disseminate fresh 3D printed concrete and discovered that the cavitation effect of PUS greatly aided in the early growth of ettringite.

Furthermore, the mechanism of PUS's cavitation effect in the cement paste is not systematically discussed in the literature that is currently available; instead, it usually concentrates on the cement hydration acceleration from the perspective of PUS. Furthermore, more investigation is required to ascertain whether the PUS treatment causes temporary or permanent cavitation.

5. Concluding remarks and future trends

The possibilities of sonication to improve dispersion in cementitious systems and affect the properties of cement-based composites have been summarized in this work. Prior research found that PUS improved pozzolanic activity by facilitating the dispersion of natural pozzolans and mineral additives in cementitious systems. The amplitude and intensity of the sonication might be changed to provide stronger sonication effects on the early strength development of cement-based composites. Entrapped air spaces in hardened cement pastes and cement suspensions were eliminated by the PUS-induced degassing action, enhancing the mechanical characteristics that followed. The PUS technology is superior to some conventional procedures in a number of ways. Advantages include low energy usage (sustainable processing), easy scaling (viability), decreased or eliminated use of hazardous solvents (greener processing), and reduced or eliminated heat (non-thermal processing). Regarding the technology's scalability and commercialization, there are still a lot of obstacles to overcome. Despite being a 'green' technology with several possible field applications and multiple proven results from lab-scale operations, there aren't many viable PUS applications being implemented at the industrial scale. The lack of scale-up techniques for reactors to fulfil industrial demands is a significant barrier to the technology's further development. Without a thorough understanding of physical and chemical phenomena, it is impossible to manage the sensitivity and vulnerability of PUS systems to operating parameters. As a result, the current study also attempts to examine the primary parameters that should be taken into account when cavitational activity intensifies. Uniform distribution of cavitational activity inside the reactor, the precise term 'Sonoreactor' [77, 78], is one of the most significant issues in the PUS treatment scale-up design. Even though these reactors have higher operating costs than conventional ones, Lisowski *et al.* [69] proposed that a sonoreactor with closed-circuit cooling may be more cost-effective because of its unique ability to regulate mixture temperatures, which advances the understanding of PUS effects on cement-based composites' hydration and strength development. The impact of sonotrode position and cycle (pulse control mode) on the cement paste treatment by PUS has not been investigated in any of the aforementioned studies. A sonoreactor's design must include energy conversion, high volume operation, process efficiency, and rates that might result in higher treatment costs. Furthermore, because it is challenging to precisely replicate the Sonoreactor geometry and PUS environment that are comparable to laboratory-scale reactors, along with an even distribution of cavitational activity, it is crucial to make sure that the design of industrial-scale sonoreactors can achieve maximum efficiency. Since scaling up the process is still a significant difficulty, this approach is now far from being completely developed. The thorough investigation and understanding of a number of critical operating parameters, including temperature, ultrasonic frequency, sonication time, irradiation intensity, and sonoreactor design, are essential to bringing the lab-scale process to the level of industrialization. Designing and developing effective power ultrasonic systems (generators and sonoreactors) that can be tailored to each unique industrial process is also crucial. A description of the cavitational activity within the sonoreactor and the geometrical aspects of the employed sonoreactor should always be documented in terms of fundamental laboratory experiments. The comparability of various setups is sadly limited by the frequent absence of key elements in literature reviews, particularly those published in non-specialist publications. As it is being developed, the state-of-the-art for defining the entire spectrum of PUS's chemical and physical impacts is still limited, even though this work compiles existing data and offers recommendations on how to employ analytical techniques to harness ultrasonic potential. A deeper understanding of the intricate physical-chemical processes that underlie PUS's activities and how they impact its functional and technological qualities will also help reinforce the potential uses of PUS technologies in the cement and concrete industry in the future. In many industrial processes, the efficient application of high-intensity PUS will have a promising future.

References

1. Scrivener K.L., Juilland P., Monteiro P.J.M., Advances in understanding hydration of Portland cement, *Cement and Concrete Research*, **78**: 38–56, 2015.

2. Scrivener K.L., John V.M., Gartner E.M., Eco-efficient cements: Potential economically viable solutions for a low-CO_2 cement-based materials industry, *Cement and Concrete Research*, **114**: 2–26, 2018.

3. Snellings R., Suraneni P., Skibsted J., Future and emerging supplementary cementitious materials, *Cement and Concrete Research*, **171**: 107199, 2023.

4. Thomas M., *Properties of Fresh Concrete; Supplementary Cementing Materials in Concrete*, pp. 57–67, CRC Press, Taylor & Francis Group, 2013.

5. Thomas M., Chapter 6: Temperature rise and risk of thermal cracking, in: *Supplementary Cementing Materials in Concrete*, pp. 69–76, CRC Press, 2013.

6. Hassan K.E., Cabrera J.G., Maliehe R.S., The effect of mineral admixtures on the properties of high-performance concrete, *Cement and Concrete Composites*, **22**: 267–271, 2000.

7. Papadakis V.G., Effect of supplementary cementing materials on concrete resistance against carbonation and chloride ingress, *Cement and Concrete Research*, **30**: 291–299, 2000.

8. Irassar E.F., Di Maio A., Batic O.R., Sulfate attack on concrete with mineral admixtures, *Cement and Concrete Research*, **26**: 113–123, 1996.

9. Xu G.J.Z., Watt D.F., Hudec P.P., Effectiveness of mineral admixtures in reducing ASR expansion, *Cement and Concrete Research*, **25**: 1225–1236, 1995.

10. Akkaya Y., Ouyang C., Shah S.P., Effect of supplementary cementitious materials on shrinkage and crack development in concrete, *Cement and Concrete Composites*, **29**: 117–123, 2007.

11. Edson A., Fowler D., Juenger M., Suh C., Won M., Effects of Supplementary Cementing Materials on the Setting Time and Early Strength of Concrete, *Technical Report by The University of Texas at Austin*, 2008.

12. Hu X., Shi Z., Shi C., Wu Z., Tong B., Ou Z., de Schutter G., Drying shrinkage and cracking resistance of concrete made with ternary cementitious components, *Construction and Building Materials*, **149**: 406–415, 2017.

13. Lothenbach B., Scrivener K., Hooton R.D., Supplementary cementitious materials, *Cement and Concrete Research*, **41**: 1244–1256, 2011.

14. Juenger M.C.G., Snellings R., Bernal S.A., Supplementary cementitious materials: new sources, characterization, and performance insights, *Cement and Concrete Research*, **122**: 257–273, 2019.

15. Skibsted J., Snellings R., Reactivity of supplementary cementitious materials (SCMs) in cement blends, *Cement and Concrete Research*, **124**: 105799, 2019.

16. Mielenz R., Witte L., Glantz O., Effect of calcination on natural pozzolans, in: *Symposium on Use of Pozzolanic Materials in Mortars and Concretes*, pp. 43–92, 1950.

17. Alujas A., Fernández R., Quintana R., Scrivener K.L., Martirena F., Pozzolanic reactivity of low grade kaolinitic clays: influence of calcination temperature and impact of calcination products on OPC hydration, *Applied Clay Science*, **108**: 94–101, 2015.

18. Almenares R.S., Vizcaíno L.M., Damas S., Mathieu A., Alujas A., Martirena F., Industrial calcination of kaolinitic clays to make reactive pozzolans, *Case Studies in Construction Materials*, **6**: 225–232, 2017.

19. Aldea C., Young F., Wang K., Shah S.P., Effects of curing conditions on properties of concrete using slag replacement, *Cement and Concrete Research*, **30**: 465–472, 2000.

20. Zhao Y., Qiu J., Xing J., Sun X., Chemical activation of binary slag cement with low carbon footprint, *Journal of Cleaner Production*, **267**: 121455, 2020.

21. Allahverdi A., Maleki A., Mahinroosta M., Chemical activation of slag-blended Portland cement, *Journal of Building Engineering*, **18**: 76–83, 2018.

22. Shi C., Day R.L., Comparison of different methods for enhancing reactivity of pozzolans, *Cement and Concrete Research*, **31**: 813–818, 2001.

23. Shi C., An overview on the activation of reactivity of natural pozzolans, *Canadian Journal of Civil Engineering*, **28**: 778–786, 2001.

24. Ganjian E., Ehsani A., Mason T.J., Tyrer M., Application of power ultrasound to cementitious materials: advances, issues and perspectives, *Materials & Design*, **160**: 503–513, 2018.

25. Lisowski P., Glinicki M.A., Novel processing methods of low-clinker multicomponent cementitious materials–A review, *Applied Sciences*, **14**(2): 899, 2024.

26. Yao Y., Pan Y., Liu S., Power ultrasound and its applications: A state-of-the-art review, *Ultrasonics Sonochemistry*, **62**: 104722, 2020.

27. Rivas D.F., Cintas P., Glassey J., Boffito D.C., Ultrasound and sonochemistry enhance education outcomes: From fundamentals and applied research to entrepreneurial potential, *Ultrasonics Sonochemistry*, **103**: 106795, 2024.

28. Martınez-Velandia D., Paya J., Monzo J., Borrachero M.V., Granulometric activation of densified silica fume (CSF) by sonication, *Advances in Cement Research*, **20**: 129–135, 2008.

29. Janca M., Siler P., Opravil T., Kotrla J., Improving the dispersion of silica fume in cement pastes and mortars, *IOP Conference Series: Materials Science and Engineering*, **583**: 012022, 2019.

30. Jafari V., Allahverdi A., Vafaei M., Ultrasound-assisted synthesis of colloidal nanosilica from silica fume: Effect of sonication time on the properties of product, *Advanced Powder Technology*, **25**: 1571–1577, 2014.

31. Fraga Y.S.B., da Rêgo S. J.H., Capuzzo V.M.S., da Andrade D.S., Morais P.C., Ultrasonication and synergistic effects of silica fume and colloidal nanosilica on the C–S–H microstructure, *Journal of Building Engineering*, **32**: 101702, 2020.

32. Nigam P., Rawat R., Pasla D., Mechanical and durability performance enhancement of recycled aggregate concrete using nano silica, *Innovative Infrastructure Solutions*, **10**: 356, 2025.
33. Elkady H., Serag M.I., Elfeky M.S., Effect of nano silica de-agglomeration, and methods of adding superplasticizer on the compressive strength, and workability of nano silica concrete, *Civil and Environmental Research*, **3**: 2, 2013.
34. Long W.-J., Liu J.-W., He C., A facile approach to disperse metakaolin for promoting compressive strength of cement composites, *Construction and Building Materials*, **404**: 133268, 2023.
35. Vaičiukynienė D., Vaitkevičius V., Jakevičius L., Kantautas A., Effect of sonication on the compressive strength of Portland cement with zeolite addition, *Cement Wapno Beton*, **20**(1): 45–52, 2015.
36. Chen J., Li W., Huang W., Chen Q., Ma Y., Zhang M., Li Z., Fu J., Ouyang X., Feasibility study of using carbonated and ultrasound treated electric arc furnace slag as a nano-enhanced supplementary cementitious material, *Cement and Concrete Composites*, **157**: 105946, 2025.
37. Tsardaka E.-C., Stefanidou M., Application of an alternative way for silica fume dispersion in cement pastes without ultrasonication, *Cement and Concrete Research*, **115**: 59–69, 2019.
38. Chatel G., Novikova L., Petit S., How efficiently combine sonochemistry and clay science?, *Applied Clay Science*, **119**: 193–201, 2016.
39. Harbec D., Tagnit-Hamou A., Gitzhofer F., Waste-glass fume synthesized using plasma spheroidization technology: Reactivity in cement pastes and mortars, *Construction and Building Materials*, **107**: 272–286, 2016.
40. Mao Y., Jiao D., Hu X., Jiang Z., Shi C., Dispersion behavior of silica fume in cementitious suspensions, *Cement and Concrete Composites*, **151**: 105605, 2024.
41. Wang X., Zeng J., Qin C., Tang D., Yang J., Zhao H., Zhou Y., Ye H., Zheng B., He X., Potential industrial approach for efficient dispersion of silica fume: Rapid wet-grinding dispersion technique, *Construction and Building Materials*, **401**: 132893, 2023.
42. Ni C., Wu Q., Yu Z., Shen X., Hydration of Portland cement paste mixed with densified silica fume: From the point of view of fineness, *Construction and Building Materials*, **272**: 121906, 2021.
43. Rodríguez E.D., Soriano L., Payá J., Borrachero M.V., Monzó J.M., Increase of the reactivity of densified silica fume by sonication treatment, *Ultrasonics Sonochemistry*, **19**: 1099–1107, 2012.
44. Wang X., Huang J., Dai S., Ma B., Tan H., Jiang Q., Effect of silica fume particle dispersion and distribution on the performance of cementitious materials: a theoretical analysis of optimal sonication treatment time, *Construction and Building Materials*, **212**: 549–560, 2019.

45. Monzo J., Martínez-Velandia D., Paya J., Borrachero M., Effect of sonication on the reactivity of silica fume in Portland cement mortars, *Advances in Cement Research*, **23**: 23–31, 2011.

46. Askarinejad A., Pourkhorshidi A.R., Parhizkar T., Evaluation the pozzolanic reactivity of sonochemically fabricated nano natural pozzolan, *Ultrasonics Sonochemistry*, **19**: 119–124, 2012.

47. Diamond S., Sahu S., Densified silica fume: particle sizes and dispersion in concrete, *Materials and Structures*, **39**: 849–859, 2006.

48. Zhang M.-H., Islam J., Peethamparan S., Use of nano-silica to increase early strength and reduce setting time of concretes with high volumes of slag, *Cement and Concrete Composites*, **34**: 650–662, 2012.

49. Rodrigues F.A., Low-temperature synthesis of cements from rice hull ash, *Cement and Concrete Research*, **33**: 1525–1529, 2003.

50. Manzur T., Yazdani N., Strength enhancement of cement mortar with carbon nanotubes. transportation research record, *Transportation Research Record*, **21**: 102–108, 2010.

51. Makar J.M., Margeson J., Luh J., Carbon nanotube/cement composites – early results and potential applications, in: *Proceedings of the 3rd international conference on construction materials: Performance, innovations and structural implications*, pp. 1–10, 2005.

52. Makar J.M., Chan G.W., Growth of cement hydration products on single walled carbon nanotubes, *Journal of the American Ceramic Society*, **92**: 1303–1310, 2009.

53. Kawashima S., Hou P., Corr D.J., Shah S.P., Modification of cement-based materials with nanoparticles, *Cement and Concrete Composites*, **36**: 8–15, 2012.

54. Xu Z.S., Ji Y.S., Ma Z.G., Xu S.N., Zhang J., Zhang Z.Z., Xue Q., Strengthening mechanism of ultrasonic action on mechanical properties of cement-based materials, *Construction and Building Materials*, **362**(2): 129788, 2023.

55. Xiong G., Ren Y., Fang Z., Jia X., Sun K., Guo B., Huang Q., Wang C., Zhou S., Understanding the cavitation effect of power ultrasound in cement paste, *Construction and Building Materials*, **438**: 137089, 2024.

56. Ehsani A., Ganjian E., Haas O., Tyrer M., Mason T.J., The positive effects of power ultrasound on Portland cement pastes and mortars; a study of chemical shrinkage and mechanical performance, *Cement and Concrete Composites*, **137**: 104935, 2023.

57. Wang J., Zhang C., Liao J., Kong X., Effect of power ultrasound treatment on cement hydration in the presence of polycarboxylate, *Construction and Building Materials*, **458**: 139493, 2025.

58. Xiong G., Wang C., Zhou S., Zheng Y., Ren Y., Fang Z., Zhao Y., Understanding the thermal effect of power ultrasound in cement paste, *Applied Thermal Engineering*, **232**: 120946, 2023.

59. Xiong G., Ren Y., Jia X., Fang Z., Sun K., Huang Q., Wang C., Zhou S., Understanding the influence of ultrasonic power on the hydration of cement paste, *Journal of Building Engineering*, **87**: 108996, 2024.

60. Xiong G., Liu S., Yang G., Zhang S., Wang C., Poon C.-s., Preparation of reactive seedings by in-situ precarbonation under power ultrasound-assisted mixing: Enhancing the hydration and mechanical properties of OPC, *Cement and Concrete Composites*, **152**: 105630, 2024.

61. Remus R., Rößler C., Peters S., Sowoidnich T., Ludwig H.-M., Fundamental effects of using power ultrasound to accelerate C_3S hydration, *Cement and Concrete Research*, **180**: 107514, 2024.

62. Ehsani A., Ganjian E., Mason T.J., Tyre M., Bateman M., Insights into the positive effects of PUS on the pore solution of Portland cement pastes, *Cement and Concrete Composites*, **125**: 104302, 2022.

63. Xiong G., Wang C., Zhou S., Zhao Y., Li Y., Liu Y., Qiu J., Effect of power ultrasound-assisted mixing on the hydration and microstructural development of cement paste, *Journal of Sustainable Cement-Based Materials*, **12**(9): 1061–1072, 2022.

64. Ehsani A., Ganjian E., Mason T.J., Tyrer M., Bateman M., Insights into the positive effects of power ultrasound on the pore solution of Portland cement pastes, *Cement and Concrete Composites*, **125**: 104302, 2022.

65. Peters S., *The Influence of Power Ultrasound on Setting and Strength Development of Cement Suspensions*, PhD Thesis, Bauhaus-Universität Weimar, 2017, https://core.ac.uk/download/pdf/224742379.pdf.

66. Mason T.J., Peters D., *Practical Sonochemistry, Power Ultrasound Uses and Applications*, 2nd ed., Woodhead Publishing, 2002.

67. Choi J., Kim T.-H., Kim H.-Y., Kim W., Ultrasonic washing of textiles, *Ultrasonics Sonochemistry*, **29**: 563–567, 2016.

68. Rashwan S.S., Dincer I., Mohany A., Investigation of acoustic and geometric effects on the sonoreactor performance, *Ultrasonics Sonochemistry*, **69**: 105174, 2020.

69. Lisowski P., Jóźwiak-Niedźwiedzka D., Osial M., Bochenek K., Denis P., Glinicki M.A., Power ultrasound-assisted enhancement of granulated blast furnace slag reactivity in cement paste, *Cement and Concrete Composites*, **154**: 105781, 2024.

70. Remus R., Roßler C., Hesse P., Nune S., Ludwig H., Power ultrasound assisted production of sustainable concrete, in: *Proceedings of the 16th International Congress on the Chemistry of Cement*, 2023.

71. Serelis E., Vaitkevicius V., Hilbig H., Irbe L., Rudzionis Z., Effect of ultra-sonic dispersion time on hydration process and microstructure development of ultrahigh performance glass powder concrete, *Construction and Building Materials*, **298**(6): 123856, 2021.

72. Lv S.H., Wu L., Li Z.X., Gao R.J., Liu L.P., Investigation of dispersion behavior of GO in aqueous and effect of ultra-low dosage GO on structure and properties of cement-based composites, *Construction and Building Materials*, **350**(3): 128828, 2022.
73. Xiong G.Q., Ren Y.L., Wang C., Zhang Z.R., Zhou S., Kuang C., Zhao Y., Guo B.M., Hong S.X., Effect of power ultrasound assisted mixing on graphene oxide in cement paste: dispersion, microstructure and mechanical properties, *Journal of Building Engineering*, **69**(15): 106321, 2023.
74. Sonocrete. A New Wave of Concrete, www.sonocrete.com.
75. Sonicators for Liquid Processing in Lab and Production, www.hielscher.com.
76. Vaitkevicius V., Serelis E., Kersevicius V., Effect of ultra-sonic activation on early hydration process in 3D concrete printing technology, *Construction and Building Materials*, **66**: 422–428, 2014.
77. Asgharzadehahmadi S., Raman A.A.A., Parthasarathy R., Sajjadi B., Sonochemical reactors: Review on features, advantages and limitations, *Renewable and Sustainable Energy Reviews*, **63**: 302–314, 2016.
78. Adamou P., Harkou E., Villa A., Constantinou A., Dimitratos N., Ultrasonic reactor set-ups and applications: A review, *Ultrasonics Sonochemistry*, **107**: 106925, 2024.

3. A Test Rig for Efficiency Measurements of Spur Gear Transmissions in a Micro-Drive System

Arkadiusz Chyliński, Wojciech J. Dera, Hubert Grzywacz,
Dariusz M. Jarząbek*

Institute of Fundamental Technological Research, Polish Academy of Sciences
Warsaw, Poland
* Corresponding Author: djarz@ippt.pan.pl

The paper presents preliminary results obtained on a laboratory test rig designed for analyzing the efficiency of spur gear transmissions. The investigated object was a simple gear pair consisting of two gears with a module of 1, made of C45 steel. The analysis covered efficiency measurements as a function of load torque and rotational speed, under both 'dry' operation and after lubrication with ŁT-4 grease. The obtained results indicate that the efficiency of the gear increased with the load torque, reaching a maximum of over 99.7 %. It was found that lubrication improved efficiency by 0.5–1 percentage points compared to dry operation, especially at higher speeds. The results confirm the correctness of the test rig operation and its suitability for further studies on different types of gears and lubrication conditions.

https://doi.org/10.24423/9788365550682.ch3

1. Introduction

Gear transmissions are among the most commonly used power transmission elements in engineering, and their efficiency significantly affects the overall performance of drive systems. In the era of device miniaturization and mechatronics development, research on small gear transmissions is gaining importance, particularly in mobile robotics, automation, and precision equipment.

The efficiency of a gear transmission depends on many factors: gear geometry, materials, manufacturing quality, lubrication conditions, and load [1]. Experimental studies are essential for verifying theoretical models of power losses.

Previous test rigs allowed the analysis of material and geometrical properties of gears efficiency [2–4]. However, those setups were relatively large, costly, and not easily adapted to educational purposes. Moreover, they were mainly intended for testing multi-stage gearboxes rather than single meshing pairs [5].

For instance, the Łukasiewicz – Institute for Sustainable Technologies in Radom has designed a number of tribological rigs for testing various types of gear systems. The T-30 test rig enables the analysis of scuffing and pitting wear mechanisms in spiral bevel gears under controlled thermal and load conditions, enabling the evaluation of gear oils and low-friction coatings [6]. Another system, the T-34 test rig, allows the measurement of start-up friction torque and friction torque under dynamically steady conditions in a climatic chamber operating from $-50\,^{\circ}\mathrm{C}$ to $+50\,^{\circ}\mathrm{C}$, making it possible to assess gear losses in extreme thermal conditions [7].

Similarly, studies carried out at Silesian University of Technology [8] have contributed to the development of experimental infrastructure for testing bevel and planetary gears, focusing on the tribological performance, load-carrying capacity, and influence of lubrication. These systems, although advanced, are typically designed for large or medium-sized gearboxes and industrial applications, often requiring high-power electric drives and complex instrumentation.

The aim of this work was to design and build a compact test rig enabling efficiency measurements of small spur gears in a micro-drive system. The paper presents the device construction, measurement methodology and exemplary test results.

2. Research methodology

The test rig was based on the classical power recirculation method, in which the energy supplied by an electric motor circulates through the test and reference gears in a closed-loop system. The flow of mechanical power in such a system is shown in Fig. 1. In the power recirculation method, power circulates between

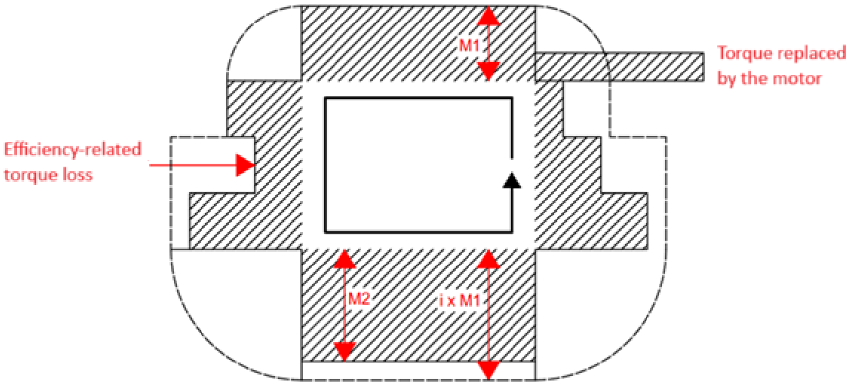

Fig. 1. Power flow in the power recirculation system.

the elements of the mechanism, being dissipated as friction and viscous losses, while the motor compensates for the losses. The mathematical description of the method was adopted from [5]. Since total losses in the mechanical system can be divided into load-dependent and load-independent components, $P_{\mathrm{total}} = P_M + P_S$ where P_M is the load-dependent power loss and P_S is the no-load loss, the use of a two-step measurement allows for their separate determination.

In the measurement with a preloaded clutch, $M_{cl} \neq 0$ the motor must overcome both types of losses, $P_{T1} = P_M + P_S$. In the measurement with an unloaded clutch, $M_{cl} = 0$ the motor compensates only for no-load losses $P_{T2} \approx P_S$. Thus, the load-dependent losses can be determined as $P_M = P_{T1} - P_{T2}$, and the meshing efficiency is calculated as:

$$\eta_m = 1 - \frac{P_M}{2 \cdot M_{\mathrm{sprz}} \cdot \omega_{\mathrm{sil}}}.$$

The division by 2 results from the load being distributed between two gears. The total system efficiency is then:

$$\eta_T = 1 - \frac{P_{T1}}{2 \cdot M_{\mathrm{sprz}} \cdot \omega_{\mathrm{sil}}}.$$

During the tests, not only the motor current was recorded, but also the temperature in the gear contact zone and, in selected cases, the acoustic emission of the system. Temperature monitoring enabled the observation of changes in operating conditions over time, which was particularly important for longer test cycles. Acoustic monitoring was considered an auxiliary parameter, providing potential for future extensions towards vibration analysis and gear condition diagnostics.

The testing procedure involved mounting the selected gear pair, applying the preload torque using a lever with weights, and starting the motor. After stabilizing the operating conditions, measurements were taken at various torque and speed values. The obtained data were used to generate efficiency characteristics as a function of load, which were then compared.

3. Test rig design

The developed test rig was designed as a compact laboratory device, with a primary focus on ease of operation and quick exchange of test gears. The construction was based on a steel frame, providing sufficient stiffness and stability during measurements. The frame carried a drive unit based on a DC motor, along with fixtures for mounting both the test and reference gears. The drive motor is an 80 W maxon motor DCX32L brushed DC unit providing a nominal torque of 120 mNm at 6640 rpm. The maximum load applied during testing has been determined at 10 Nm at the stationary gear shaft.

Special attention was given to the precise adjustment of the center distance, achieved using a linear guide enabling smooth displacement of one module. The screw used to alter the axis distance is equipped with a locknut, ensuring preload stability under vibration conditions. The other half of the screw has been manufactured to tight tolerances, making sure any play present is omittable. This solution allowed for testing different gears without major modifications to the setup. The overall concept was inspired by the FZG test machine, widely used for similar research [9], and described in detail in [10].

The measurement system was integrated with the structure in a simple and reliable manner. Efficiency calculations were based on measuring the current drawn by the motor, which eliminated the need for strain gauge torque sensors, significantly simplifying and reducing the cost of the rig. Additionally, the setup provided for temperature monitoring in the contact zone via an IR temperature sensor and noise level measurement via a MEMS microphone, offering opportunities for future expansion. For lubrication, a peristaltic pump was implemented to dose grease in a controlled and repeatable way, ensuring stable test conditions and enabling comparative studies of different lubricants. By extending the measurement time and applying cyclic torque loads, the test rig can serve as a platform for investigating fatigue damage and wear processes in small gear pairs.

Despite its laboratory scale, the rig was designed with ergonomics and modularity in mind, allowing for straightforward replacement of test gears and future modifications, such as extending the load range or adding more measurement channels. The CAD model of the device is shown in Fig. 2, while the prototype is presented in Fig. 3.

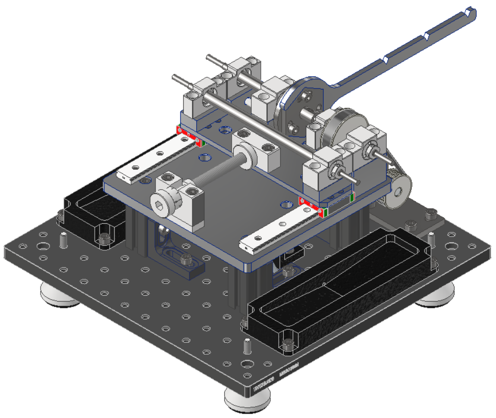

Fig. 2. CAD model of the device.

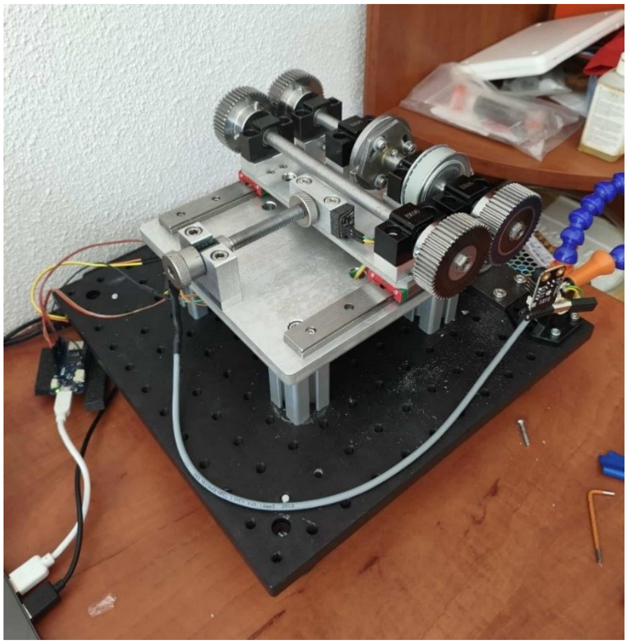

Fig. 3. Prototype of the test rig.

4. Test results – sample gear transmission

To verify the correct operation of the test rig, preliminary measurements were carried out using a spur gear pair made of C45 steel, with 48 teeth each and a module of 1. This was the smallest gear size that could be tested on the rig. The geometry was selected to replicate operating conditions typical of small drive systems. A photograph of the tested gears is presented in Fig. 4.

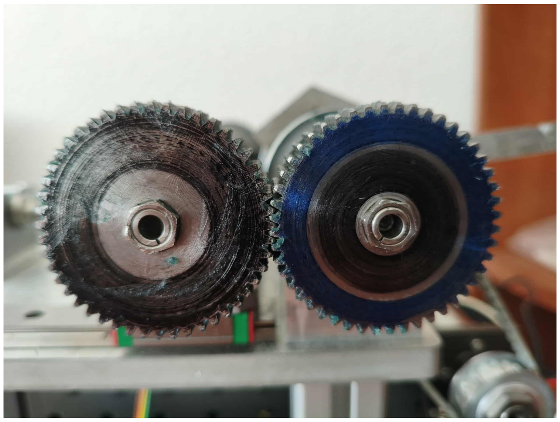

Fig. 4. Tested spur gear pair.

Measurements were performed at various load torque and speed values to determine efficiency characteristics. Each measurement involved motor startup, speed, and temperature stabilization, followed by recording motor current, gear contact temperature, and acoustic variations. Input and output powers were then calculated, and gear efficiency was determined. Table 1 presents efficiencies under dry conditions, while Table 2 shows results after lubrication with ŁT-4 grease. In both cases, efficiency increased with load torque. Under dry conditions, efficiency decreased at higher speeds, while lubrication maintained values above 99 % across a wide speed range. Data were collected for approximately 30 seconds at each operating point and averaged.

Table 1. Efficiency results under dry operation.

Dry operation						
M_sprz [Nm]	1.15	4.35	5.5	1.15	4.35	5.5
in [RPM]	n_m [%]			n_t [%]		
50	98.73	99.05	99.67	97.20	98.56	99.29
100	98.80	99.09	99.66	97.13	98.55	99.25
200	98.78	99.07	99.62	96.87	98.45	99.15
300	98.46	98.95	99.55	96.39	98.28	99.05
400	97.99	98.77	99.33	95.89	98.09	98.82
500	97.64	98.55	99.13	95.51	97.86	98.61

Table 2. Efficiency results under lubricated operation (ŁT-4 grease).

Lubricated operation (ŁT-4)						
M_sprz [Nm]	1.15	4.35	5.5	1.15	4.35	5.5
in [RPM]	n_m [%]			n_t [%]		
50	99.34	99.43	99.77	97.79	98.92	99.39
100	99.45	99.55	99.79	97.82	99.02	99.39
200	99.46	99.56	99.83	97.74	99.00	99.41
300	99.44	99.52	99.77	97.46	98.87	99.29
400	99.35	99.41	99.74	97.27	98.73	99.23
500	99.16	99.31	99.63	96.96	98.59	99.09

Figures 5 and 6 show efficiency characteristics as a function of rotational speed, at different torque values. It can be clearly seen that efficiency increases with load torque. Under dry operation, efficiency decreased with increasing speed, whereas under lubrication, a peak efficiency occurred at medium speeds, followed by a decrease at higher speeds. This behavior is consistent with typical gear transmission characteristics, where frictional losses dominate at low loads, but decrease with increasing torque. At very high speeds, the hydrodynamic effects of the lubricant become the main source of losses.

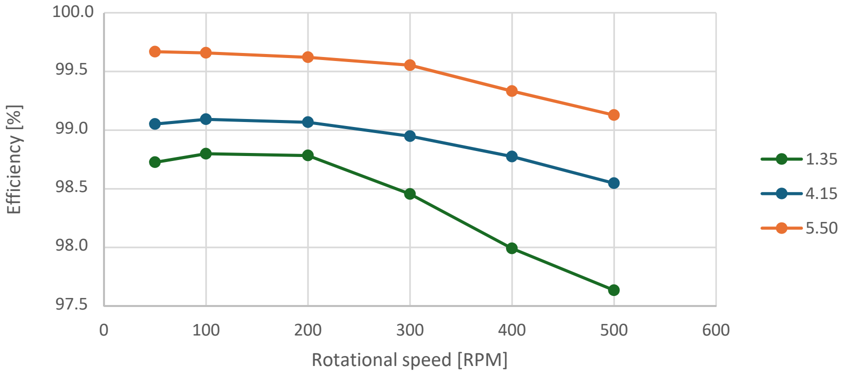

Fig. 5. Efficiency as a function of the rotational speed during dry operation.

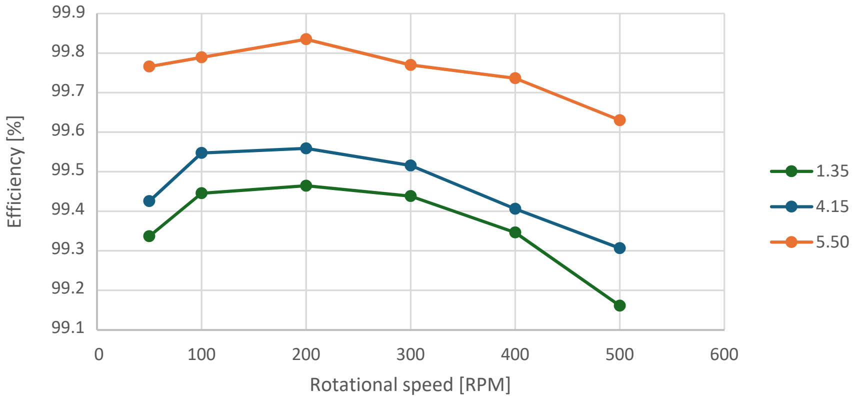

Fig. 6. Efficiency as a function of the rotational speed during lubricated operation.

5. Discussion

The conducted tests confirmed the correct operation of the test rig and the consistency of the obtained characteristics with theoretical predictions and literature reports [2, 5, 11]. It was shown that gear efficiency increases with load torque, resulting from the decreasing relative contribution of frictional losses [2].

The comparison of dry and lubricated operation demonstrated that ŁT-4 grease significantly improves gear performance, particularly by reducing boundary friction losses and stabilizing the load transfer in the meshing zone. At the same time, at the highest speeds, a drop in efficiency was observed due to increasing viscous losses in the lubricant, consistent with observations by other authors [5, 11].

Temperature and acoustic analyses confirmed stable operation of the gear pair under all tested conditions. The absence of anomalies indicated correct meshing conditions and proper manufacturing quality of the gears.

The obtained results should be considered preliminary. The study was limited to spur gears with a small module; thus, further research should include gears with different modules, helix angles, and lubricants. An interesting direction would also be a comparison between spur and helical gears, where axial forces and friction conditions differ significantly.

6. Conclusions

The objective of this study was to validate the developed test rig by analyzing the efficiency of spur gears with a module of 1, made of C45 steel. The obtained results confirmed both the functionality of the measurement system and its capability to perform tests over a wide range of speeds and loads.

The conducted experiments showed that:

- gear efficiency increases with load torque due to the decreasing relative share of frictional losses at higher loads,
- under dry conditions, efficiency decreases with speed, while under lubrication, a maximum occurs at medium speeds, with a decrease at high speeds caused by viscous losses,
- lubrication with ŁT-4 grease improved efficiency by 0.5–1 percentage points compared to dry operation, clearly demonstrating its beneficial influence on gear operation,
- acoustic and temperature measurements confirmed stable operation throughout the tested range, with no indications of meshing irregularities.

In summary, the developed test rig enables obtaining reliable efficiency characteristics of spur gears and forms a solid basis for further comparative studies. Future work should be extended to other gear types (helical, bevel), different materials, and various lubricants, providing a broader dataset for design analysis and better representation of operational conditions.

References

1. Skoć A., *Podstawy konstrukcji maszyn. Tom 3. Przekładnie mechaniczne*, 1st ed., Wydawnictwo Naukowe PWN, Warszawa, 2018.
2. Petry-Johnson T.T., Kahraman A., Anderson N.E., Chase D.R., An experimental investigation of spur gear efficiency, *Journal of Mechanical Design*, **130**: 062601, 2008, https://doi.org/10.1115/1.2898876.
3. Niza M.E. *et al.*, Test rig for micro gear and experimental analysis on the meshing condition and failure characteristics of steel micro involute gear and metallic glass one, *Mechanism and Machine Theory*, **45**(12): 1797–1812, 2010, https://doi.org/10.1016/j.mechmachtheory.2010.08.008.

4. Anderson N.E., Loewenthal S.H., *Spur-Gear-System Efficiency at Part and Full Load*, Technical Paper 1622, NASA, Cleveland, OH, 1980.
5. Chase D.R., Development of an efficiency test methodology for high-speed gearboxes, Master's thesis, The Ohio State University, 2005.
6. Tuszyński W., Kalbarczyk M., Michalak M., Badania tribologiczne kół zębatych stożkowych. Cz. I – Urządzenie i metodyka badawcza, *Tribologia*, **242**(2): 83–96, 2012.
7. Tuszyński W. *et al.*, New test rig for measuring the friction torque of gearboxes in extreme thermal conditions, *Tribologia*, **296**(2): 57–64, 2021, https://doi.org/10.5604/01.3001.0015.5869.
8. Michalczewski R. *et al.*, The effect of a gear oil on abrasion, scuffing, and pitting of the DLC-coated 18CrNiMo7-6 Steel, *Coatings*, **9**(1): 2, 2019, https://doi.org/10.3390/coatings9010002.
9. International Organization for Standardization, Gears – FZG test procedures – Part 1: FZG test method A/8,3/90 for relative scuffing load-carrying capacity of oils, ISO 14635-1:2023(en), 2023.
10. Chyliński A., Konstrukcja urządzenia do pomiaru sprawności przekładni zębatych, Engineering thesis, Politechnika Warszawska, Warszawa, 2025.
11. Li X., Sosa M., Andersson M., Olofsson U., A study of the efficiency of spur gears made of powder metallurgy materials – ground versus super-finished surfaces, *Tribology International*, **95**: 211–220, 2016, https://doi.org/10.1016/j.triboint.2015.11.021.

4. Thick Chromium Atomic Force Microscopy Probes: Fabrication and Comparative Study

Hanna Konopacka[1], **Hubert Grzywacz**[1], **Dariusz M. Jarząbek**[1,2*]

[1] Faculty of Mechatronics, Institute of Micromechanics and Photonics,
Warsaw University of Technology
Warsaw, Poland
[2] Institute of Fundamental Technological Research, Polish Academy of Sciences
Warsaw, Poland
[*] Corresponding Author: djarz@ippt.pan.pl

We present a report on the fabrication and characterization of chromium–nickel atomic force microscopy (AFM) probes with a chromium-coated tip and a bi-metallic cantilever. The introduction of a chromium layer enhances tip hardness and wear resistance, while nickel improves adhesion and reduces brittleness, enabling higher probe usability. The fabrication process was optimized through careful substrate polishing, photoresist selection, and stress control in chromium deposition, which limited the maximum chromium thickness to ∼1 µm. Mechanical testing confirmed that the probes operate reliably in AFM, achieving imaging quality comparable to commercial silicon probes, though resolution was constrained by the relatively large tip radius. Importantly, the design allows for tailoring of stiffness and resonance frequency by adjusting nickel thickness, broadening the applicability of the probes for both contact and intermittent-contact AFM modes. These results establish a proof-of-concept for durable metallic AFM probes engineered for tribological and high-load applications.

Keywords: atomic force microscopy (AFM), chromium–nickel probes, metallic cantilevers, probe fabrication, wear resistance, tip stiffness, tribological testing.

https://doi.org/10.24425/9788365550682.ch4

1. Introduction

Miniaturization is one of the major technological trends observed worldwide [1]. Along with smaller devices, such as micro-electro-mechanical systems

MEMS [2], there comes a need for a more sophisticated understanding of micro- and nano-scale behaviour. Such understanding should provide the ability to anticipate device failure. One of the approaches for small-scale material characterization is Atomic Force Microscopy AFM, in use since 1986 [3]. The most common setup includes a silicon probe, which proved to be useful for a high number of applications [4]. However, one should be aware that some problems depend on mutual interactions between the sample and probe. Thus, the material of the probe's tip should be chosen based on the requirements of a given application. Examples where this is a crucial aspect of the experiment design are: friction coefficient measurement [5, 6], adhesion [5, 6], and wear [7]. Notably, yet another issue is the experimental range of such parameters as the maximum force or resonance frequency of the AFM probe. A method that provides a broadening of the range of materials, stiffness, and tip shapes was shown in [8]. So far, it has been used for preparing an all-metal cantilever, but made from a single element. Augmenting this approach for a two-elemental system may have benefits such as higher stiffness, better adhesion of consequent layers of metal as well as increased hardness of the tip.

In this work, we showed an improved use of the abovementioned approach to provide a chromium tip with a chromium-nickel cantilever. A chromium tip has been chosen to further improve the wear resistance of the apex of the tip. The chromium-nickel cantilever has been designed for higher stiffness than the pure nickel cantilever. The addition of nickel also reduced brittleness, thereby increasing usability. The main result of this work is the successful fabrication of a chromium-tip, chromium-nickel cantilever AFM probe and its proof-of-concept in a simple tribological test.

2. Experimental

2.1. Probes design

One of the main advantages of the all-metal probes is a possibility to design a cantilever for a specific stiffness. A nominal stiffness and resonance frequency for given cantilever dimensions were calculated as follows:

- Effective Young's modulus E_{eff} for bi-material cantilever:

$$E_{\mathrm{eff}} = \frac{E_{\mathrm{Ni}} \cdot I_{\mathrm{Ni}} + E_{\mathrm{Cr}} \cdot I_{\mathrm{Cr}}}{I_{\mathrm{tot}}}, \tag{1}$$

  where E_{Ni} and E_{Cr} are Young's moduli of Ni and Cr, respectively, and I_{Ni}, I_{Cr}, and I_{tot} are moments of inertia of Ni part of the cross-section, Cr part of the cross section, and the total cross-section of the cantilever. The geometry of the cantilever is defined as shown in Fig. 1.

- The effective density ρ_{eff} for a bi-material cantilever:

$$\rho_{\mathrm{eff}} = \frac{\rho_{\mathrm{Ni}} \cdot V_{\mathrm{Ni}} + \rho_{\mathrm{Cr}} \cdot V_{\mathrm{Cr}}}{V_{\mathrm{tot}}}, \tag{2}$$

  where ρ_{Ni} and ρ_{Cr} are densities of Ni and Cr, respectively, and V_{Ni}, V_{Cr}, and V_{tot} are volumes of Ni part, Cr part, and the total of cantilever.

- Theoretical stiffness k_{eff} and resonance frequency $\omega_{0\mathrm{eff}}$:

$$k_{\mathrm{eff}} = \frac{E_{\mathrm{eff}} \cdot b \cdot h^3}{4 \cdot L^3}, \tag{3}$$

$$\omega_{0\mathrm{eff}} = \frac{\lambda_0^2}{2\sqrt{3}} \cdot \sqrt{\frac{E_{\mathrm{eff}}}{\rho_{\mathrm{eff}}}} \cdot \frac{h}{L^2} \cdot \frac{1}{2\pi}, \tag{4}$$

  where λ_0 – constant equal to $0.596864 \cdot \pi$.

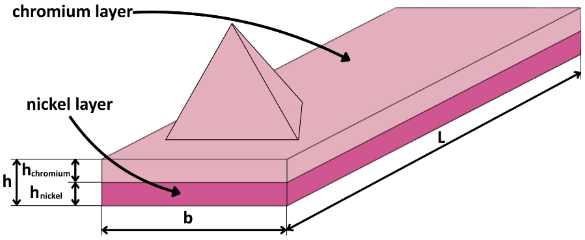

Fig. 1. Geometry of the designed chromium–nickel cantilever with chromium coating on the tip. Dimensions used for stiffness and resonance frequency calculations are indicated.

The Young modulus and theoretical density are determined by the choice of materials; however, the fabrication design can influence k_{eff} and $\omega_{0\mathrm{eff}}$ through the cantilever geometry. As shown in Table 1, an appropriate choice of dimensions enables the design of probes suitable for both contact and intermittent-contact AFM modes. The calculations were performed for a fixed cantilever length of 450 µm and a chromium layer thickness of 1 µm.

2.2. Probes fabrication

An experimental fabrication process was conducted as shown in Fig. 2.

In step 1, a sacrificial substrate is polished to a mirror finish. Step 2 is indenting the substrate to prepare a mold for the cantilever's tip. Step 3 consists of photoresist deposition on the substrate with dimensions equal to the dimensions of the cantilever and its base. Step 4 is an electrodeposition of Cr for a designed thickness with subsequent deposition of nickel, aiming for a designed total thickness. One should note that after this step, a tip is prepared from nickel as well

Table 1. Calculated stiffness and resonance frequency of chromium–nickel cantilevers for various nickel thicknesses and widths (chromium layer thickness fixed at 1 µm).

For the chromium–nickel cantilever			
Width b [µm]	Nickel thickness h [µm]	Stiffness k [N/m]	Resonance frequency ω_0 [kHz]
20	0.25	0.028	5.895
50	0.25	0.071	5.895
200	0.25	0.282	5.895
20	0.5	0.047	6.828
50	0.5	0.117	6.828
200	0.5	0.468	6.828
20	0.75	0.072	7.765
50	0.75	0.18	7.765
200	0.75	0.721	7.765
20	1	0.105	8.705
50	1	0.263	8.705
200	1	1.051	8.705
20	2	0.335	12.475
50	2	0.838	12.475
200	2	3.353	12.475
20	5	2.526	23.809
50	5	6.316	23.809
200	5	25.264	23.809
20	10	15.131	42.712
50	10	37.827	42.712
200	10	151.308	42.712

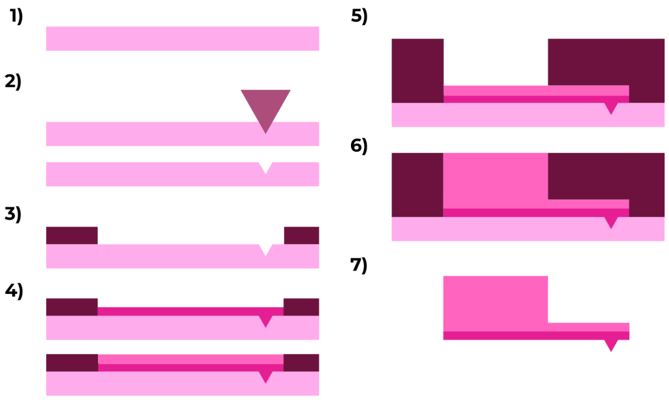

Fig. 2. Schematic of the fabrication process: (1) substrate polishing, (2) tip mold preparation by indentation, (3) photoresist deposition, (4) chromium and nickel electrodeposition, (5) mold preparation for base, (6) nickel deposition of base, (7) substrate removal.

as the whole Cr-Ni cantilever. The following steps include: 5 – preparing a thick photoresist layer as a mold for a cantilever base; 6 – electrodeposition of nickel to fill that mold. Finally, step 7 is etching a sacrificial substrate to reveal the tip, cantilever and base.

This approach resulted in a tip with increased hardness, better adhesion of the first (Cr) layer to the second (Ni) layer than for the Ni–Ni interface, and higher stiffness. For chrome deposition, Chrome Plating Solution (dr Galva, Germany) with the following parameters: temperature = 25 °C, voltage = 3 V, current density = 24 A/dm2, and time = 220 s. Initially, the rest of the parameters were the same as in [8]. However, for improving the quality of the fabricated cantilevers, the process was optimized and a comparison of initial and final results will be shown as well as the final fabrication process.

3. Probes testing

Probes were tested after each fabrication step with optical microscopy (DSX 500, Olympus, Japan) or scanning electron microscopy (Zeiss Crossbeam 350, Zeiss, Germany). For performance testing of the ready-to-use probe, AFM (Flex-AFM, Nanosurf, Switzerland) was used. Comparison with the commercially available HQ:CSC17/Al BS (MikroMasch, USA) silicon probe was carried out on the O-doped NbN sample. AFM data were treated in the Gwyddion open-source software.

4. Results

4.1. Polishing

The substrate roughness is a direct predictor of the roughness of the as-deposited metal. The first deposited layer (step 4 in Fig. 2) forms the backside

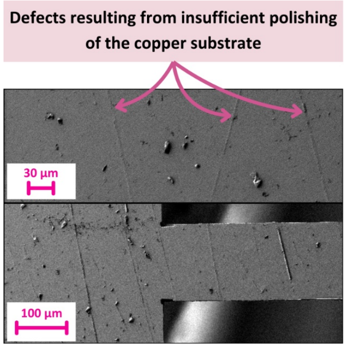

Fig. 3. Polished substrate surface. Smoother finish ensures reduced cantilever backside roughness and improved AFM laser reflection.

of the cantilever, which reflects the laser beam. Therefore, low surface roughness *Sa* is required to ensure a high-quality laser signal. However, since *Ra* and *Sa* are statistical parameters, they may not fully capture local surface imperfections. Inadequate polishing of the substrate can lead to residual material irregularities, which are then reproduced in the deposited layers. Such imperfections, if located near the tip mold on the front side of the cantilever (step 2 in Fig. 2), may strongly deteriorate the probe quality. For this reason, each cantilever is inspected for polishing-related defects, as shown in Fig. 3.

5. Photoresist

One of the crucial steps of the fabrication of metal probes is the photoresist deposition of the substrate. Details of this process are shown in Fig. 4.

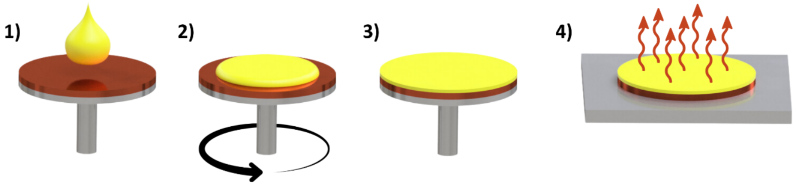

Fig. 4. Process of photoresist deposition: 1) droplet application on the substrate, 2, 3) spin-coating for uniform distribution, and 4) soft-baking for stabilization of the layer.

In step 1 photoresist droplet is deposited on the substrate. Step 2 is centrifuging this droplet by rotating the substrate. As the smooth layer of photoresist covers the substrate, in the final step, the whole system is soft-baked for 1 min at 80 °C and then for 15 min at 135 °C. The rotation speed was selected according to the photoresist thickness characteristics provided by the manufacturer and was set to 1500 rpm, which resulted in a layer thickness of 50 μm. With this result, the photoresist thickness can be chosen according to the desirable cantilever thickness.

Yet another issue connected with photoresist is its chemical resistivity. In the earlier work, it was shown that AZ 15nXT photoresist can be readily used with a Ni electrodeposition bath as a suitable mask. Preliminary tests with Cr electrodeposition bath showed that this photoresist is highly deteriorated during the process (Fig. 5a). Chemically resistant AZ125-10B was used, both without (Fig. 5b) and with additional baking (Fig. 5c). Results for Cr structures are shown in Fig. 5.

Changing the photoresist to AZ125-10B as well as applying additional baking led to a significant increase in the quality of electrodeposited Cr structures. This allows this process to be used to fabricate cantilevers. Fabrication of the third photoresist layer for AFM probes presents several challenges. Substrate preparation takes about an hour, and exposure can last up to thirteen hours,

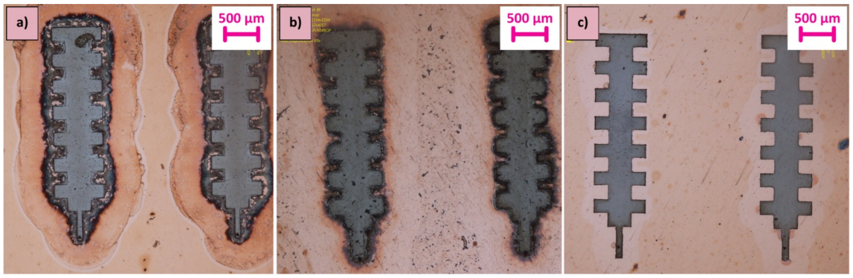

Fig. 5. Effect of photoresist selection during chromium electrodeposition: a) AZ 15nXT degraded, b) AZ125-10B stable, c) AZ125-10B with additional baking. The optimized process yielded high-quality chromium layers.

making it difficult to maintain stable environmental conditions. Variations in temperature and humidity lead to uneven resist thickness and defects. Selecting the correct exposure energy is critical: too low energy results in incomplete cross-linking, while too high energy can cause cracking or stress.

Common failure modes include (Fig. 6): a) electrolyte penetration beneath the photoresist, which can be minimized by proper exposure energy; b) pho-

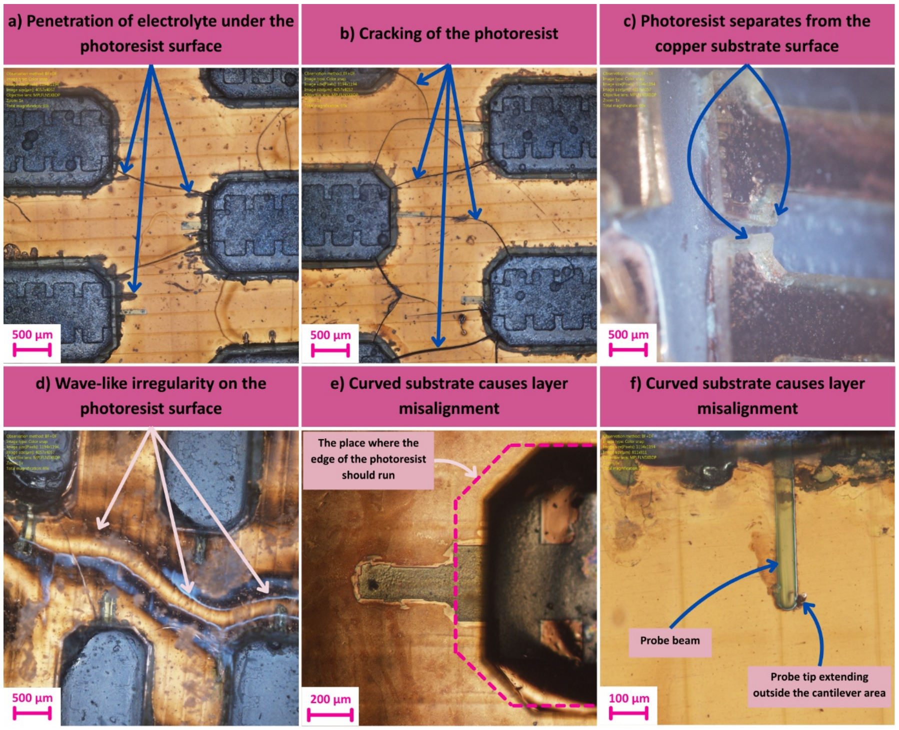
a) Penetration of electrolyte under the photoresist surface

b) Cracking of the photoresist

c) Photoresist separates from the copper substrate surface

d) Wave-like irregularity on the photoresist surface

e) Curved substrate causes layer misalignment

f) Curved substrate causes layer misalignment

The place where the edge of the photoresist should run

Probe beam

Probe tip extending outside the cantilever area

Fig. 6. Example of photoresist defects observed during fabrication of the third photoresist layer for AFM probes.

toresist cracking, controlled by adjusting the exposure dose; c) photoresist separation from the copper substrate, prevented by thorough surface cleaning and optimized exposure; d) wave-like surface irregularities, reduced by selecting the appropriate resist thickness and exposure parameters; e) substrate warping causing layer misalignment, addressed through careful attachment before polishing; and f) substrate warping causing layer misalignment, addressed through careful detachment after polishing.

Even minor defects in the mask can significantly affect probe geometry, making precise control of the process essential.

6. Tip-mold

Typically, the indentation impression perfectly resembles the indentation tip shape as well as other indentation-related phenomena. This leads to the visible re-creation of a pile-up pattern of the deposited metal, as shown in Fig. 7a.

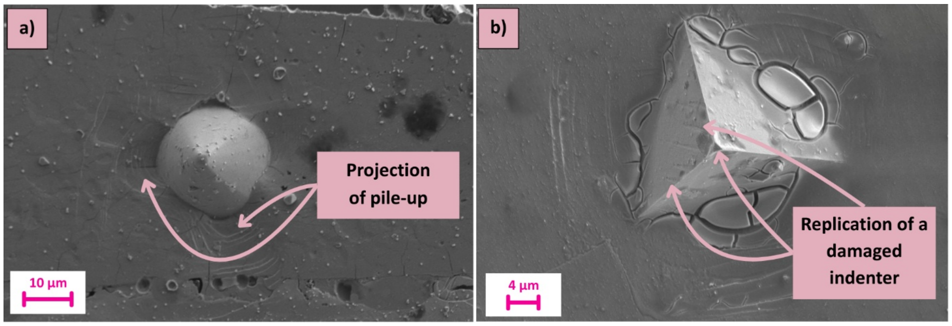

Fig. 7. Tip defects resulting from a blunted indenter during mold preparation.

This effect may be mitigated by lowering the indentation force as well as changing the indenter shape. However, it should be noted that pile-ups are significantly lower than the height of the nominal impression. Another reason for inspecting the tip of as-received cantilever is indentation tip blunting. The result of damaged indentation tip on the cantilever's tip is shown in Fig. 7b.

It can be seen that the very apex of the tip is of irregular shape. It means that the indentation tip for tip molding should be renewed. Yet another possible issue with tip molding is residual photoresist in the mold before metal deposition, as described in Fig. 8.

This problem occurred when the removal of untreated photoresist was too fast. Successful removal of the photoresist from the bottom of the 15 µm tip impression was achieved by using an acetone bath in an ultrasonic cleaner for 15 minutes.

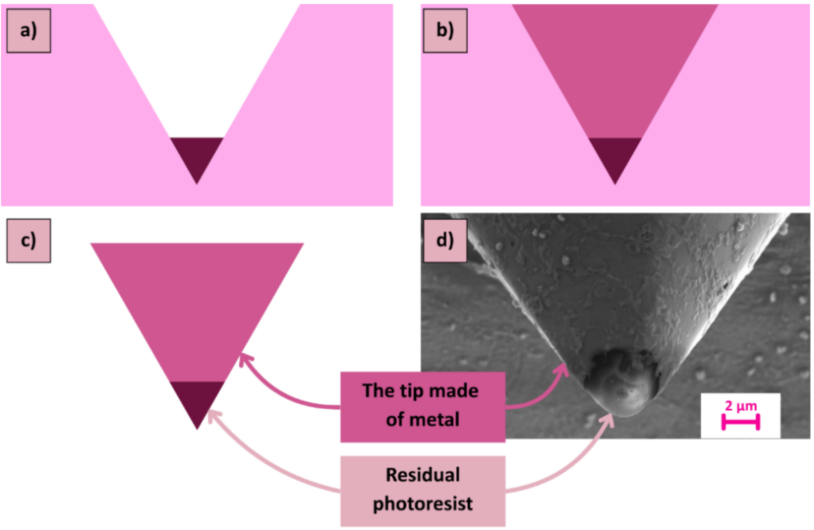

Fig. 8. Tip-mold defects caused by residual photoresist: a) photoresist remaining in the mold, b) metal electrodeposition with residual resist trapped at the bottom of the mold, c) after substrate etching the residual resist formed the tip instead of metal, d) optical image of a probe with residual photoresist on the tip.

7. Bi-layer cantilever

Initially, we intended to fabricate cantilevers with a wide range of Cr and Ni thicknesses ratio. However, Cr coating with a thickness over 1 µm proved to be highly internally stressed, as shown in Fig. 9.

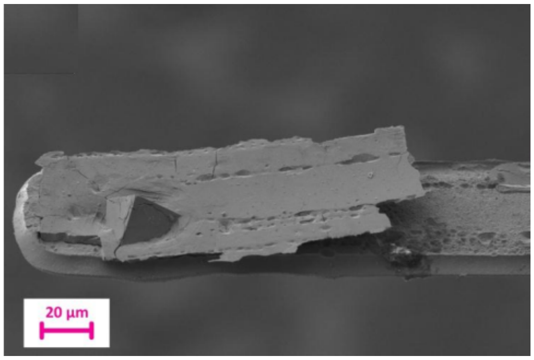

Fig. 9. Scanning electron micrograph of chromium–nickel cantilever showing intact bilayer structure with chromium thickness limited to ∼1 µm to prevent delamination.

Such stresses led to the detachment of the Cr layer from Ni the layer. Restricting the fabrication process to the Cr layer not thicker than 1 µm led to intact cantilevers. However, those cantilevers should also meet other requirements. The most basic function of the cantilever is to apply a normal force for tip-sample interaction. Being able to control that process means that back-side of the cantilever has to reflect the laser beam into the four-quadrant diode. This can happen only for a sufficiently smooth surface. In Fig. 10, the OM images of the nickel surface of the back-side of the cantilever are shown in the as-deposited state as well as after mechanical polishing.

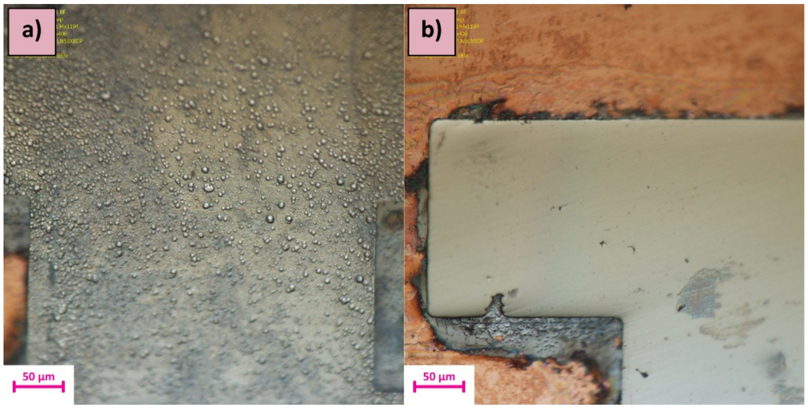

Fig. 10. Optical micrographs of nickel cantilever backside: a) as-deposited surface with high roughness, b) polished surface enabling laser reflection.

Adding a polishing step is an important change compared to the original process flow. Here, the surface roughness of as-deposited Ni on Cr was significantly higher than for all-Ni cantilevers. Mechanical polishing was carried out with 1 µm diamond suspension. Such an approach led to slow material removal, which provided control over the resulting thickness of deposited Ni as well as the small roughness needed for laser reflection.

8. Cantilever testing

With the successful fabrication of Cr-Ni AFM probes, mechanical testing in AFM was carried out. The probe used for those tests is shown in Fig. 11.

Measurements were carried out with the fabricated chromium–nickel probe using a Nanosurf Flex AFM, as shown in Fig. 12a, while Fig. 12b presents a reference measurement obtained with a commercial silicon probe. Although the images acquired with the chromium–nickel probe are not of the highest resolution, they remain comparable to those obtained with silicon probes. This limitation is mainly attributed to the relatively large tip radius of the fabricated probe.

The result of roughness Sa on the O-doped NbN sample for both Si and Cr-Ni AFM probes is shown in Fig. 13.

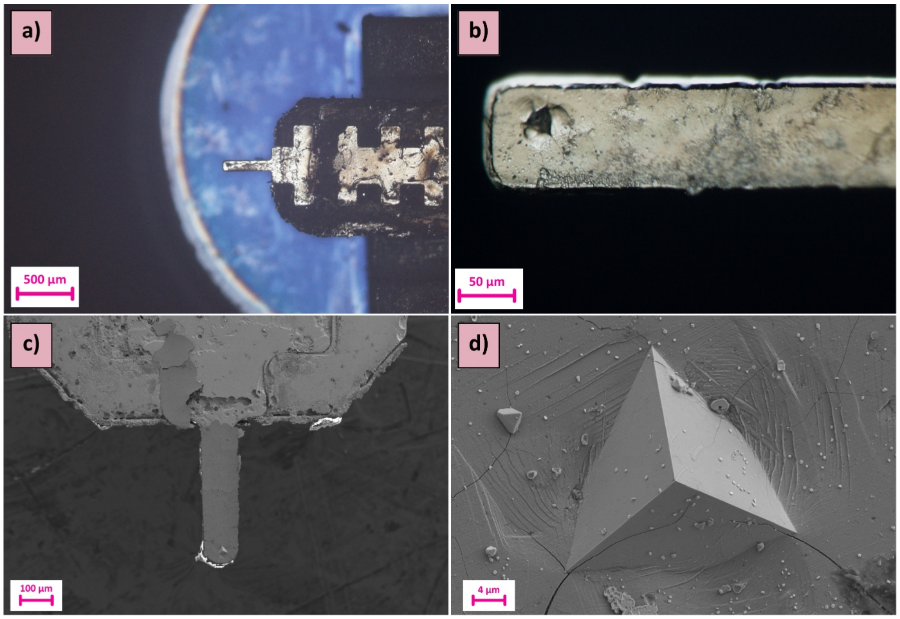

Fig. 11. Images of fabricated chromium–nickel probes: a, b) optical microscope images of completed probes, and c, d) scanning electron microscopy (SEM) images of fabricated probes.

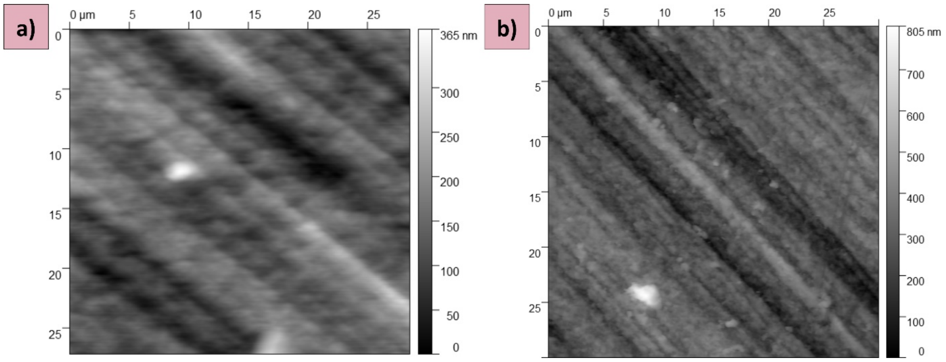

Fig. 12. AFM measurements of O-doped NbN sample: a) acquired using the fabricated chromium–nickel probe, b) reference measurement obtained with a commercial silicon probe.

Statistical analysis of the surface roughness measurements yielded a mean $Sa = 94.2 \pm 27.8\,\text{nm}$ for the chromium–nickel probe and $Sa = 65.3 \pm 1.2\,\text{nm}$ for the silicon probe ($n = 63$ and $n = 66$, respectively). While the chromium–nickel probe exhibited a higher measurement dispersion, this behavior reflects its increased stiffness and robustness, which makes it suitable for high-load and tribological AFM applications. Despite the larger tip radius, the chromium–nickel probe provided imaging quality comparable to the silicon probe and demon-

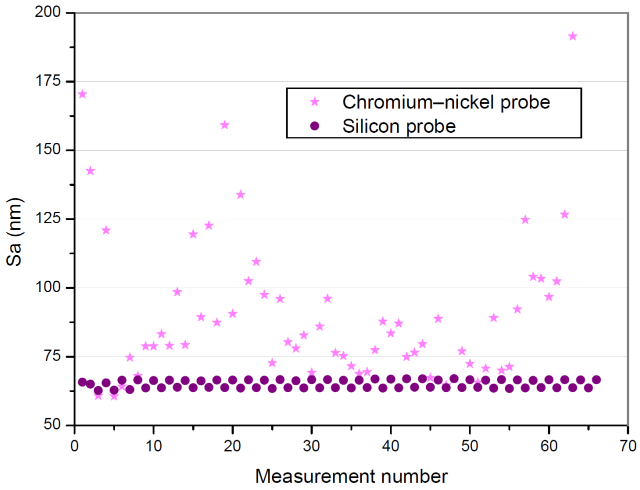

Fig. 13. Comparison of surface roughness (Sa) values measured on O-doped NbN sample using chromium–nickel probe and commercial silicon probe.

strated mechanical durability which enables stable operation under demanding measurement conditions.

9. Discussion

The fabrication of chromium–nickel AFM probes presented here demonstrates both the feasibility and challenges of extending bi-metallic approaches to the AFM probe design. The introduction of a chromium layer at the tip region improved wear resistance, while the nickel underlayer mitigated brittleness and facilitated adhesion between layers. Nevertheless, several fabrication challenges were encountered, particularly stress accumulation in thick chromium coatings. These stresses limited the maximum practical chromium thickness to approximately 1 µm, which constrained the design space. The necessity of additional polishing steps further underscores the sensitivity of the optical readout to surface roughness, highlighting that the introduction of chromium requires process modifications compared with all-nickel probes.

The successful operation of chromium–nickel probes in AFM measurements confirmed that they can reach imaging quality comparable to that of commercial silicon probes. While the resolution was limited by the relatively large tip radius, the tribological benefits of chromium – particularly hardness and wear resistance – are expected to enhance probe longevity in demanding applications. The fabrication approach also demonstrated flexibility: by tuning nickel thickness, a wide range of cantilever stiffness values and resonance frequencies can be achieved, offering opportunities for tailoring probes to specific experimental requirements. However, scaling the process and ensuring reproducibility remain open issues. Variability in photoresist stability, substrate preparation, and tip-mold definition will need to be systematically addressed before the probes can become competitive alternatives in routine AFM applications.

10. Conclusions

We have demonstrated a chromium–nickel AFM probe architecture that combines a chromium tip with a nickel-supported cantilever. This design improves hardness, adhesion and stiffness while maintaining functional imaging capability comparable to silicon probes. Although fabrication challenges – particularly stress management in chromium layers – currently limit process robustness, the concept opens a pathway towards durable metallic probes tailored for high-load and tribological AFM experiments. Future refinements in tip shaping and stress control should enable probes with both higher resolution and enhanced longevity, broadening the experimental scope of AFM in materials science and nanotechnology.

Although the fabricated Cr–Ni probes exhibited slightly higher roughness dispersion compared to commercial silicon probes, their durability and resistance to wear make them promising for high-load or tribological AFM applications.

Acknowledgements

This research was supported by the National Centre for Research and Development (Poland) grant TANGO-IV-B/0002/2019.

References

1. Pattanaik P., Ojha M., Review on challenges in MEMS technology, *Materials Today: Proceedings*, **81**(Part 2): 224–26, 2023, https://doi.org/10.1016/j.matpr.2021.03.142.
2. Yellampalli S. [Ed.], *MEMS Sensors: Design and Application*, IntechOpen, 2018, https://doi.org/10.5772/intechopen.71153.
3. Binnig G., Quate C.F., Gerber Ch., Atomic force microscope, *Physical Review Letters*, **56**(9): 930–933, 1986, https://doi.org/10.1103/PhysRevLett.56.930.
4. Voigtländer B., *Atomic Force Microscopy*, 2nd ed., Springer Nature, Cham, 2019, https://doi.org/10.1007/978-3-030-13654-3.
5. Bhushan B. [Ed.], *Nanotribology and Nanomechanics: An Introduction*, 4th ed., Springer International Publishing, Cham, 2017, https://doi.org/10.1007/978-3-319-51433-8.

6. Butt H.-J., Cappella B., Kappl M., Force measurements with the atomic force microscope: Technique, interpretation and applications, *Surface Science Reports*, **59**(1–6): 1–152, 2005, https://doi.org/10.1016/j.surfrep.2005.08.003.
7. Gnecco E., Meyer E., *Fundamentals of Friction and Wear on the Nanoscale*, 2nd ed., Springer International Publishing, Cham, 2024.
8. Milczarek M., Jarząbek D.M., Jenczyk P., Bochenek K., Filipiak M., Novel paradigm in AFM probe fabrication: Broadened range of stiffness, materials, and tip shapes, *Tribology International*, **180**: 108308, 2023, https://doi.org/10.1016/j.triboint.2023.108308.

5. Flow Patterns of Two-Phase Systems in Microfluidic Cross-Junctions

Tetuko Kurniawan[1,3], **Mahsa Sahebdivani**[2],
Slawomir Blonski[1], **Piotr M. Korczyk**[1]

[1] Institute of Fundamental Technological Research, Polish Academy of Sciences
Warsaw, Poland
[2] Institute of Physical Chemistry, Polish Academy of Sciences
Warsaw, Poland
[3] President University
Cikarang Baru, Bekasi, Indonesia
* Corresponding Author: piotr.korczyk@ippt.pan.pl

This study investigated two-phase flow patterns in microfluidic cross-junctions at low capillary numbers. Four distinct flow patterns were observed: at-Junction, Downstream, Parallel Flow, and Bi-modal. The occurrence of these patterns depends on the flow rate ratio and channel aspect ratio. A novel Bi-modal pattern was discovered, where two droplet formation modes appeared alternately to produce droplets of two distinct sizes, challenging the conventional understanding of uniform droplet generation. This pattern arises from the interplay between the droplet-phase thread length, its receding dynamics, and the channel geometry. These findings expand our understanding of droplet formation mechanisms in microfluidic devices and may enable novel applications in drug delivery, material synthesis, and diagnostics.

Keywords: microfluidics, cross-junction, flow-focusing device, droplet formation, two-phase flow.

https://doi.org/10.24425/9788365550682.ch5

1. Introduction

Droplet microfluidics, a specialized branch of microfluidics, has transformed biomedical applications by enabling precise high-throughput techniques for single-cell analysis [1, 2], drug delivery [3], and point-of-care diagnostics [4]. This method leverages multiphase flow to create droplets – tiny, isolated compartments formed by immiscible fluids, typically oil and water – within microscale channels on chips. Droplets range in size from nanoliters to a few microliters and act as miniature reactors capable of isolating and encapsulating cells, molecules, or nanoparticles for controlled experiments [5]. Their small volumes reduce reagent consumption, minimize waste, and allow rapid and efficient mixing of fluids for various chemical and biochemical processes [6, 7].

Microfluidic devices can generate and manipulate thousands of droplets per second with remarkable consistency and efficiency. These droplets facilitate complex operations, such as mixing [8], merging [9], splitting [10, 11], sorting [12, 13], and trapping [14]. By combining these operations, advanced protocols such as on-demand concentration gradient generation [15] and droplet digital counting [16] can be achieved, significantly expanding the scope of droplet microfluidics applications.

At the heart of a droplet microfluidic device is a droplet generator that produces a micro-sized volume of liquid in a non-immiscible liquid. The most common type of droplet generator is a passive-type, in which droplets are generated based on the interaction between two (or more) immiscible fluids flowing through a junction of two or more channels. In the area of single-cell analysis, for example, microfluidic junctions such as co-flow, T-junction, and flow-focusing are commonly used to produce monodisperse droplets with sizes ranging from a few tens to hundreds of microns for high-throughput cell culture experiments [17].

A thorough mechanistic understanding of droplet formation is essential for the effective use of microfluidic junctions in various applications. In particular, droplet volume control requires careful consideration of flow conditions, channel geometry, and fluid properties. Because the dimensions of microchannels typically range from a few tens to a few hundreds of micrometers, conventional body forces, such as gravity and inertia, have only a minor effect on the flow. Instead, fluid behavior at this scale is dominated by the interplay between viscous and interfacial forces. To capture this balance, the capillary number (Ca) is commonly used, representing the ratio of viscous forces to interfacial forces.

In multiphase systems involving two immiscible fluids, variations in the capillary number alone can give rise to at least ten distinct flow patterns [18]. The range of possible patterns expands further when additional factors are introduced, such as the geometry of the microfluidic junction [19] and wetting properties of the liquid–surface interface [20]. These considerations highlight the inherent complexity of multiphase flow in microfluidic channels and underscore the importance of understanding the physical mechanisms governing droplet generation.

For flow patterns that produce droplets, it is widely accepted that fixed flow inputs generate monodisperse droplets – droplets with uniform size. This phenomenon has numerous applications, the most common of which is as a tool for single-cell analysis [21]. However, our research demonstrates that by subtly modifying the hydrodynamic junction geometry, it is possible to produce two or more distinct droplet sizes using fixed flow inputs, without incorporating additional active control elements.

In this unique flow pattern, two different droplet formation modes alternate, resulting in the production of two (or more) consistent droplet sizes. We have termed this pattern 'Bi-modal' owing to its characteristic dual-size output. This study aims to provide a comprehensive description and analysis of this novel flow pattern, exploring its mechanisms, potential applications, and implications for microfluidic technology.

The discovery of the Bi-modal pattern challenges the conventional understanding of droplet generation in microfluidic systems and opens up new possibilities for precise control over the droplet size distribution. That is, two or more droplet size distributions can be produced precisely without any additional control elements for the flow input, whereas previously, only a single droplet size distribution could be produced from such a system.

2. Materials and methods

2.1. Experimental setup

Five microfluidic cross-junction devices were fabricated in-house for the purpose of this study. The chip is made of two polycarbonate (PC) plates (Macrolon). Channels were engraved on both plates using the CNC milling machine (Ergwind MFG 4025P), which has a resolution of 5 µm. The two plates were bonded together using a hot press at 135 °C for 12 min. There was no modification to the surface of the microfluidic channel. Each device has rectangular cross-section channels with a constant aspect ratio, as shown in Table 1.

Table 1. Dimensions of the five chips prepared for the study of the droplet formation. W and H are the width and height of the channel, respectively. The device aspect ratio, W/H, is defined as the ratio between the width and height of the channel.

Width W [µm]	Height H [µm]	Aspect ratio W/H [–]
2010	494	4.07
1510	495	3.05
955	469	2.04
752	525	1.43
501	525	0.95

As illustrated in Fig. 1, the continuous phase (CP) and droplet phase (DP) liquids were delivered using separate computer-controlled syringe pumps (Cetoni Nemesys) loaded with 1 mL glass syringes (ILS 2624016) or 500 µL glass syringes (Hamilton 81220). Each syringe pump controlled the flow rate of the

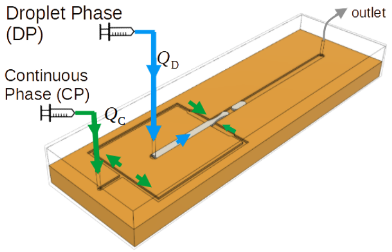

Fig. 1. Schematic of the experimental setup for droplet formation in a cross-junction device.

CP and DP, which are denoted as Q_C and Q_D, respectively (see Fig. 1). The CP and DP fluids were hexadecane 95 % (Sigma Aldrich) and fluorinated oil FC-40 (3M), respectively. The fluid pairs were chosen to ensure the wetting condition of the PC surface channel with CP without the need for a surfactant. Thus, the effect of the surfactant was excluded. The interfacial tension between the CP and DP, γ, is 7.3 N/m, which was measured using the pendant drop method at 21 °C. The viscosities of hexadecane and fluorinated oil are $\mu_C = 3.6\,\mathrm{mPa\cdot s}$ and $\mu_D = 4.1\,\mathrm{mPa\cdot s}$, respectively, as measured using a falling-ball viscometer at 21 °C. Initially, testing was performed at the lowest flow rates to ensure that no flow fluctuations were caused by the mechanical components of the pump within the range of parameters investigated in this study [22]. The syringes were connected to the inlets of the devices using polyethylene (Beckton-Dickinson PE-60) or polytetrafluoroethylene (Bola S1810-10) tubing. The same tubing was used to connect the outlet of the chip to the waste container.

2.2. Image acquisition

A stereo microscope (Zeiss Stemi 508) equipped with a CCD camera (IDS UI-3274LE-C-HQ) was used to observe the droplet formation. In the high temporal and spatial resolution experiments intended to observe the formation process at the junction, the recording frame rate was set to 45 fps. For experiments to measure droplet length and observe various flow patterns, a frame rate between 1 and 20 fps was used, depending on the flow rate of the DP. In a device with a high aspect ratio and a very low flow rate, the period between droplet pinch-off can be longer than 30 min, or in other words, approximately one hour per droplet. Thus, low frame rate recording reduces the video file size and does not affect the measurements in these experiments.

2.3. Image processing

The recorded images were analyzed using a script written in the Python 3 programming language, utilizing various packages supporting image analysis [23, 24]. The typical droplet image analysis procedure (algorithm) is as follows:

1. An RGB image was flattened into a grayscale image, as shown in Fig. 2a.
2. If a background image containing an empty junction is available, the interface of a forming droplet can be easily extracted by subtracting the intensity of the droplet-containing image from the background image, as shown in Fig. 2b.
3. If the background image is not available, it can be produced using another image processing technique. In the case of a bright-field image with uniform light coming from the back of the chip, a background image can be created by taking the maximum intensity from many images with different droplet positions. Because the interface of a droplet is a shadow (low-intensity value), the interface is replaced with higher-intensity pixels from other images.

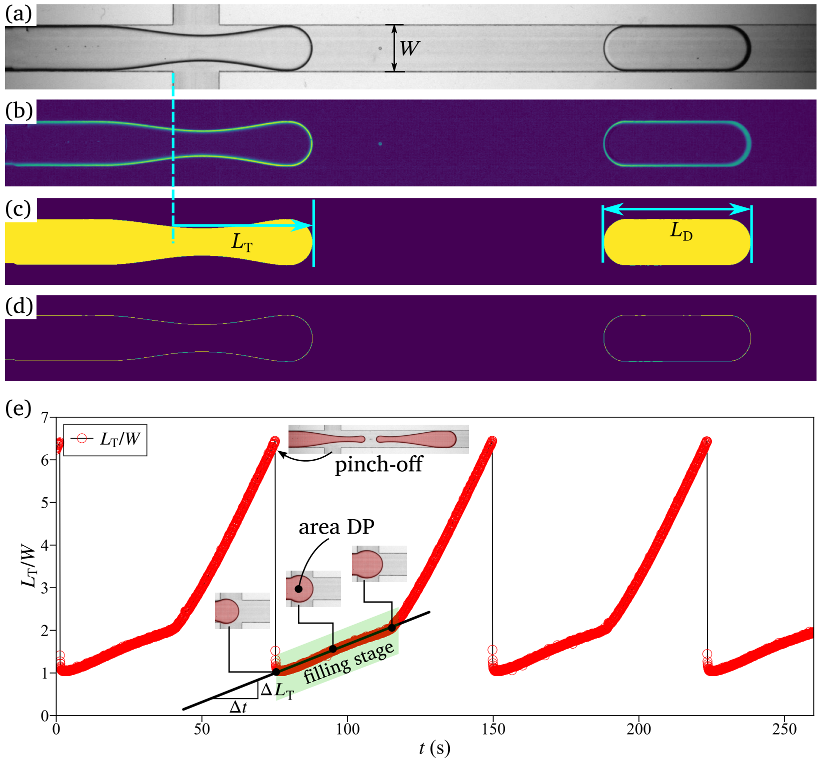

Fig. 2. Example of image processing result: (a) original grayscale image, (b) image containing the droplet shadow only as a result of subtraction with the background image, (c) image containing a filled droplet (these images were useful for measuring the droplet area), (d) image containing an outline of the droplets is useful for measuring the parameters obtained from the interface, (e) measurement result of L_T versus time. A jump in L_T marks the pinch-off of the droplet formation. In the filling stage, the droplet flows into the junction at the rate of the DP flow rate, Q_D. Thus, the increase in the droplet area is equal to Q_D/H, as illustrated in the three images with the shaded areas. Images were sourced from [25].

4. The grayscale droplet image was then converted into a binary image by applying a threshold value.
5. Image noise was reduced by executing one or a combination of morphological operations, such as erosion, dilation, opening, closing, and removal of small objects.
6. After noise removal, the resulting image contained only a droplet outline (Fig. 2d), and various parameters were measured. If required, the area enclosed by the outline can be filled by replacing the zero values within the outline with a binary value of 1, as shown in Fig. 2c.

The exact implementation of the algorithms varies depending on the quality of the recorded images. An example of the resulting measurement of the droplet tip position, L_T, is shown as red circles in Fig. 2e.

A jump in the L_T value indicates a pinch-off. Following the pinch-off, the DP recedes into the cross-junction and starts to grow at a rate proportional to the filling rate of the DP, that is, $\frac{dL_T}{dt} \propto \frac{Q_D}{HW}$. More accurately, the filling rate of the DP can be approximated by measuring the area within the growing droplet over time (see images with a red overlay). The rate of change in the droplet area is approximately equal to Q_D/H. This method can be used to verify the DP flow rate, Q_D.

3. Results and discussion

3.1. Flow patterns at low Ca regime

Multiple flow patterns can arise when two immiscible fluids flow through microfluidic junctions. The emergence of these patterns depends on the channel geometry, relative magnitudes of the two liquid flow rates, and physical properties of the fluids, such as viscosity and interfacial tension.

Consider a cross-junction device (see Figs. 1 or 2), where the droplet phase (DP) enters with a flow rate of Q_D and encounters the continuous phase (CP) with a flow rate of Q_C. The flow at this length scale and within a confined space is dominated by viscous and interfacial forces, which are captured by the Capillary number,

$$\mathrm{Ca} = \frac{\mu_C Q_C}{\gamma W H}, \tag{1}$$

where μ_C is the viscosity of the CP, γ is the interfacial tension, and W and H are the channel width and height, respectively.

The behavior of droplet formation strongly depends on Ca [18]. At higher Ca, the viscous drag from the CP is sufficient to deform the DP without requiring the DP to occupy the junction. Droplet breakup then occurs via the dripping or jetting mechanism, producing droplets smaller than the channel width [19]. In contrast, at low Ca, the droplet formation occurs only after the DP grows large enough to obstruct the outlet channel. This obstruction causes the CP to accumulate, squeezing the DP and eventually breaking it into a droplet larger than the channel width. This mechanism is known as *squeezing* droplet formation, and it depends on the junction geometry [26]. Bi-modal droplet generation is also geometrically dependent and has been found in this low Ca regime. Therefore, the present study focuses exclusively on the low Ca regime. Since only a single fluid pair is used in this study, μ_C and γ are constants. Thus, Ca depends on the device aspect ratio (see Table 1) and the CP flow rate, Q_C. In this study, the operating CP flow rate ranges from $0.01\,\mathrm{mL/h}$ to $14\,\mathrm{mL/h}$, covering Ca values between 7×10^{-6} and 5×10^{-3} across different devices.

Within this Ca regime, a variety of flow patterns emerge as a function of the ratio between two flow rates:

$$q = \frac{Q_D}{Q_C}. \tag{2}$$

These results are summarized in flow pattern maps (see Fig. 3), where the key control parameter is the flow rate ratio in combination with the channel aspect ratio, W/H. Four distinct flow patterns were observed:

1. **at-Junction**: For small q, the CP pinches off the DP near the junction, causing the DP thread to recede into the inlet channel (see blue regions in Figs. 3a–f).
2. **Downstream**: At an intermediate q, droplet pinch-off occurs further downstream. After pinch-off, the receding DP thread remained inside the outlet channel, leading to a different breakup mechanism (see orange regions in Figs. 3a–f).
3. **Parallel Flow**: For a higher q, the CP flow was insufficient to deform and break the DP. Instead, the two phases flow side by side, forming a stable filament (see green regions in Fig. 3a–f).
4. **Bi-modal**: In a narrow range of q, both at-Junction and Downstream modes appear alternatingly, producing droplets of two distinct sizes. This occurs primarily in channels with the cross-sectional aspect ratio, W/H, equal to or larger than two, as indicated by the yellow-cross markers in Figs. 3d–f.

As shown in Figs. 3b–f, the flow pattern map is unique for each device aspect ratio. This implies that the transitional flow rate ratio depends on the device W/H. The transitional flow rate ratio between Parallel Flow and Downstream is denoted as $q_{P\to D}$, while the transitional flow rate ratio between Downstream (including Bi-modal) and at-Junction is denoted $q_{D\to J}$. As shown in Figs. 3g and 3h, both $q_{P\to D}$ and $q_{D\to J}$ decrease with increasing device aspect ratio. We observed that the inverse of $q_{P\to D}$ was linearly proportional to the device aspect ratio, which is in agreement with the previous report by Humphry *et al.* [27].

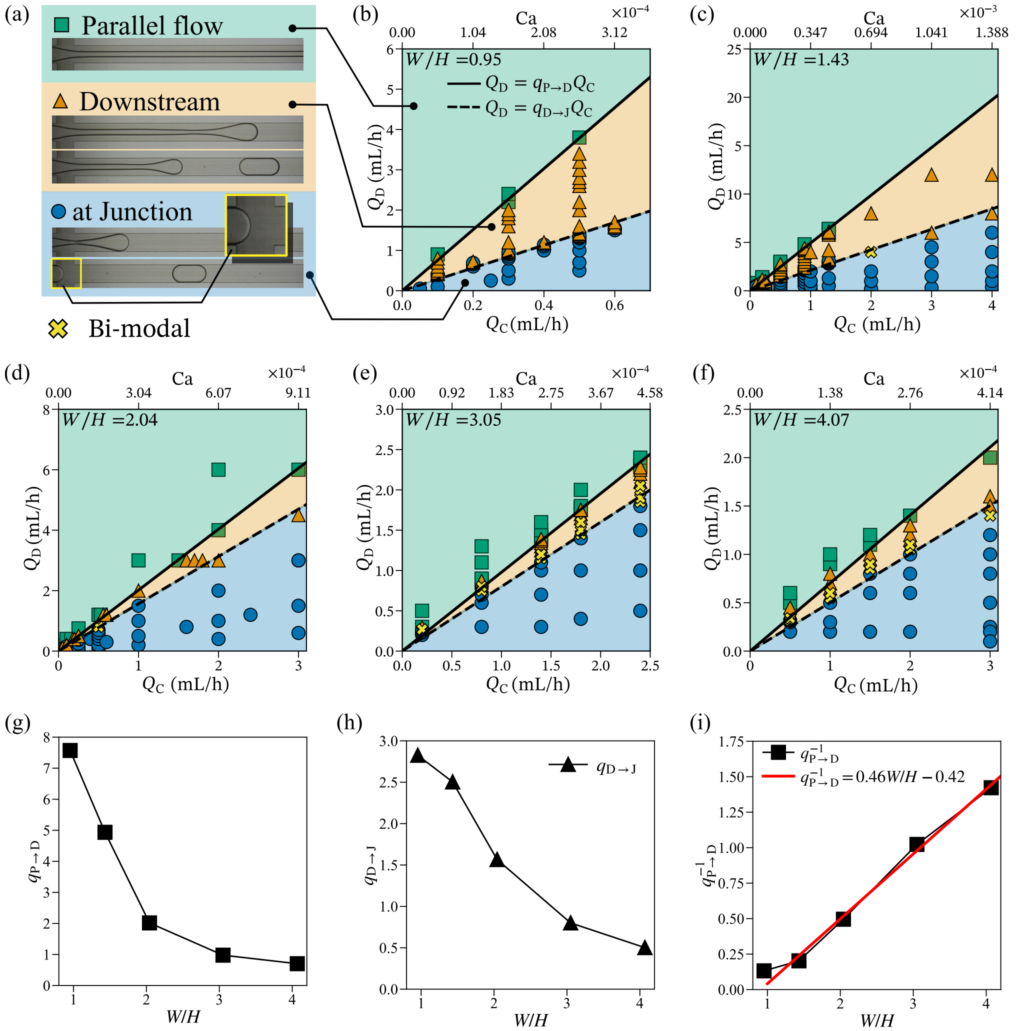

Fig. 3. Observation of flow patterns in the low-Ca flow regime: (a) flow pattern emerging owing to different flow-rate ratios, (b)–(f) flow pattern maps for different device aspect ratios, (g) $q_{P\to D}$ and (h) $q_{D\to J}$ decrease with increasing device aspect ratio W/H, (i) Linear proportionality of the inverse of $q_{P\to D}$ against W/H. Images (a)–(f) were adapted and images (g)–(i) were reproduced from [28].

3.2. Droplet formation – at-Junction

Three-dimensional images illustrating the droplet formation process in the cross-junction device with W/H of one and four are shown in Figs. 4a and 4b, respectively. The experimental images of at-Junction droplet formation are shown in Fig. 4c. From the image sequence, parameters such as the droplet tip length L_T and the local maxima and minima of droplet E were measured and plotted over

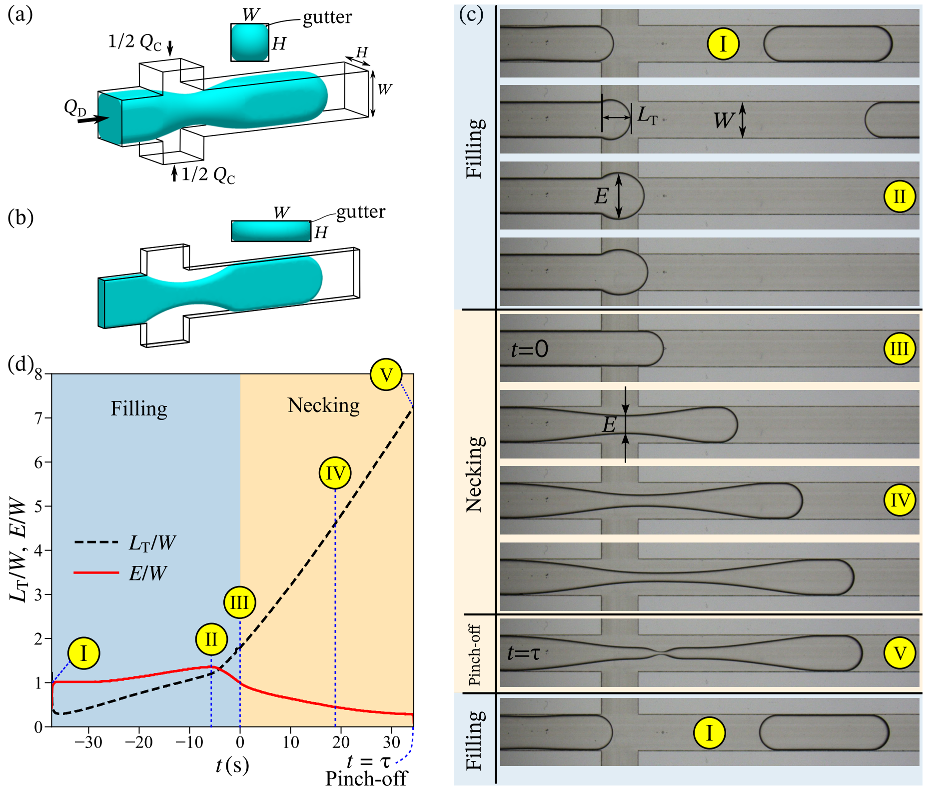

Fig. 4. Three-dimensional illustration of droplet formation in a cross-junction with W/H: (a) 1 and (b) 4. (c) Evolution of the droplet tip L_T and local maxima/minima of the forming droplet, E, in a single droplet formation cycle. (d) at-Junction droplet formation stages: filling, necking, and pinch-off. The filling stage ends when the DP blocks the outlet channel and attains a straight droplet shape, $E \approx W$. The necking time is taken from the end of the filling stage $t = 0\,\mathrm{s}$ up to pinch-off $t = \tau$. Experimental images and measurements were obtained from the device with $W/H = 4.07$ at $Q_C = 1.00\,\mathrm{mL/h}$ and $Q_D = 0.30\,\mathrm{mL/h}$. Images (a), (b), and (d) were reproduced, and image (c) was adapted from [28].

time, t (Fig. 4d). As shown in the image sequence, at-Junction droplet formation consists of three stages:

- **Filling.** This is the stage when the DP flows through the junction and has not yet occupied the outlet channel. The CP flows through the junction and directly to the outlet channel with minimal interference from the DP. Eventually, the DP becomes sufficiently long to fill the junction and outlet channels. The end of the filling stage is marked when the droplet becomes a straight plug, $E \approx W$, as shown by the II markings in Figs. 4c and 4d.
- **Necking**. Time zero of the necking stage is taken when the DP forms a straight plug, as shown by the III markings in Figs. 4c and 4d. As the

DP occupies the outlet channel and blocks the path for the CP, it increases the flow resistance for the CP flow passing through the droplet. Consequently, the CP accumulated upstream of the droplet tip and began to squeeze the DP. This process is called necking (see IV in Figs. 4c and 4d). The necking process ends when the neck of the droplet becomes thin enough to become unstable owing to the Plateau–Rayleigh instability.

- **Pinch-off**. The instability drives the collapse of the thin neck, producing a droplet of DP (see V in Figs. 4c and 4d). This process occurs in a very short time and is called the pinch-off.

3.3. Droplet formation – Downstream

The Downstream droplet formation process is similar to the at-Junction mode, except that because of the higher flow rate ratio, necking occurs much further downstream of the junction, as shown in Fig. 5a. After pinch-off, the

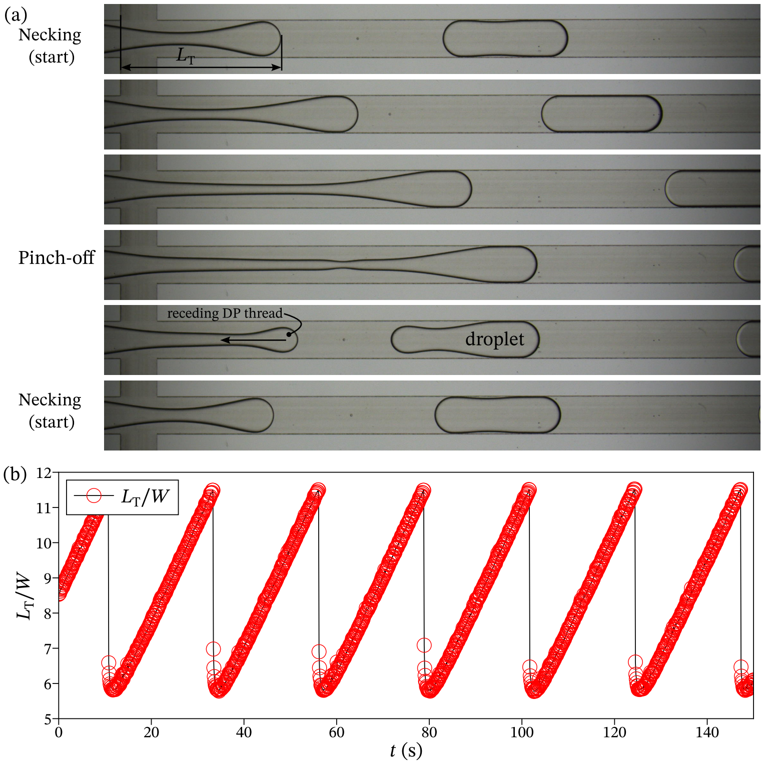

Fig. 5. (a) Downstream droplet formation occurs in two stages: necking and pinch-off. (b) Droplet tip length cycle shows that the process begins with the relaxation of the DP thread, continues with the necking phase, and concludes with the pinch-off. Experimental images and measurements were obtained from the device with $W/H = 4.07$ under flow conditions of $Q_C = 1.50\,\text{mL/h}$ and $Q_D = 0.90\,\text{mL/h}$. Images were sourced from [25].

droplet thread (i.e., the droplet phase that is part of the DP supply line) recedes and stops inside the outlet channel. The process is then followed by the necking stage, skipping the filling stage. Thus, the Downstream droplet formation consisted of only two stages: necking and pinch-off, as shown in Fig. 5a. The measurement of L_T in this mode (see Fig. 5b) also shows that after the jump (pinch-off), L_T evolves almost linearly with time until it jumps again. This is in contrast to the evolution of L_T in the at-Junction mode (Fig. 4d), where there are two different regions of L_T evolution.

3.4. Bi-modal droplet formation

Bi-modal droplet formation consists of two formation modes: at-Junction and Downstream. The two modes appeared alternately, as shown in the image sequence in Fig. 6. The image sequence with green (dark) and brown (light) backgrounds shows the at-Junction and Downstream modes, respectively. Initially, the droplet undergoes the normal at-Junction droplet formation process: filling, necking, and finally pinch-off. However, because the thread is sufficiently long, the receding thread after pinch-off remains inside the outlet channel. Next,

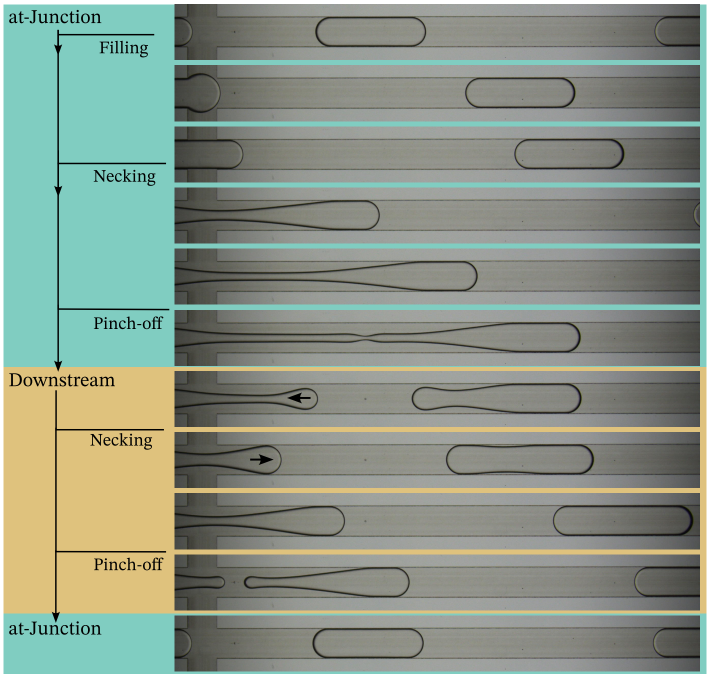

Fig. 6. Image sequence of one full cycle of bi-modal droplet formation. At-Junction (green) is followed by Downstream (brown), and then followed again by at-Junction (green). Images were captured from the device with $W/H = 4.07$ at $Q_C = 0.50\,\mathrm{mL/h}$ and $Q_D = 0.20\,\mathrm{mL/h}$. Images were sourced from [25].

the thread grows inside the channel while undergoing necking until pinch-off. The key to the process that allows the alternating condition between two modes is that there must be a sufficient length of droplet thread during at-Junction droplet formation, such that the receding thread after the pinch-off stops inside the outlet channel, allowing subsequent droplet formation in the Downstream mode. However, the droplet thread (resulting from the at-Junction mode) cannot be too long; otherwise, only cycles of the Downstream droplet formation can occur.

The two modes produced two distinct droplet sizes. The droplet size produced in the at-Junction mode was larger than that produced in the Downstream mode. This is because the overall droplet formation duration is shorter in the Downstream mode, as shown by the measurement of L_T in Fig. 7a. The evolution of L_T clearly indicates the alternating modes, with the green and brown regions appearing alternately, showing the at-Junction and Downstream modes, respectively. The at-Junction mode takes a longer time – shown by the wider green

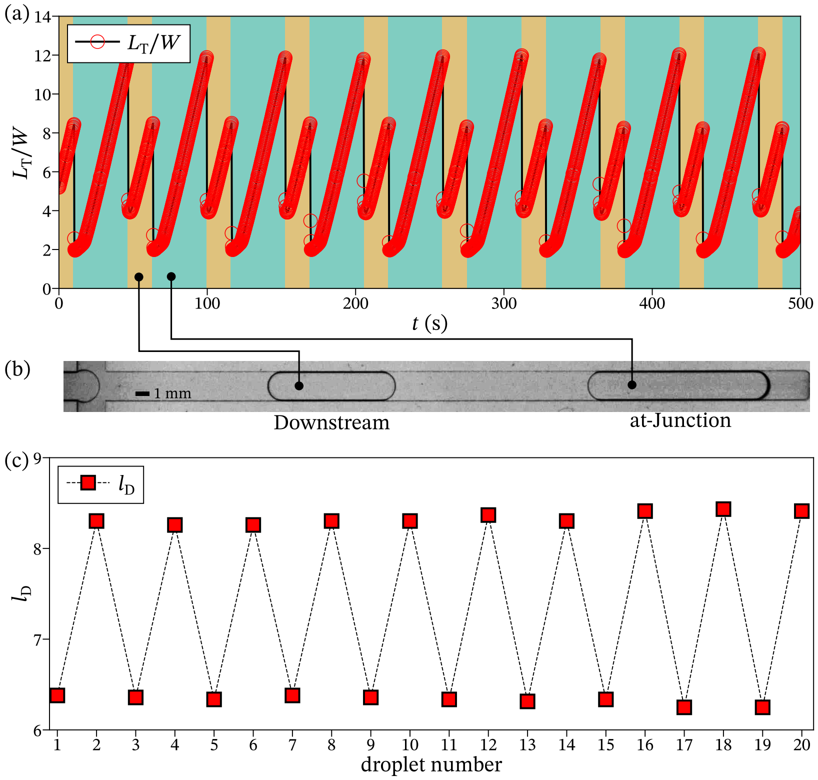

Fig. 7. (a) Evolution of L_T shows two modes of droplet formation: at-Junction (green) and Downstream (brown). (b) Experimental image showing two distinct droplet sizes. (c) Sequential pattern of two different droplet sizes. Measurements were taken from the device with $W/H = 4.07$ at $Q_C = 1.50\,\mathrm{mL/h}$ and $Q_D = 0.85\,\mathrm{mL/h}$. Images were sourced from [25].

area in Fig. 7a – because each cycle consists of filling and necking stages. Because the time for droplet formation was longer, the size of the droplet produced by the at-Junction mode was larger (see Fig. 7b). The Downstream mode only has cycles of the shorter necking stage, producing a smaller droplet size. The measurement shown in Fig. 7c shows the sequential alternating of two droplet sizes.

4. Conclusions

This study provides a comprehensive analysis of two-phase flow patterns in microfluidic cross-junction devices, focusing on the low capillary number regime. Four distinct flow patterns were identified: at-Junction, Downstream, Parallel Flow, and Bi-modal. The transitions between these patterns were found to depend on both the flow rate ratio and channel aspect ratio. Of particular interest is the novel Bi-modal pattern, which produces alternating droplet sizes under fixed flow conditions. This pattern challenges the conventional understanding of droplet generation in microfluidic systems and opens up new possibilities for precise control over the droplet size distribution.

This study provides detailed insights into the mechanisms of droplet formation for the at- Junction, Downstream, and Bi-modal patterns. The at-Junction mode consists of three stages (filling, necking, and pinch-off), whereas the Downstream mode involves only necking and pinch-off. The Bi-modal pattern alternates between these two modes, resulting in the production of two distinct droplet sizes. This unique behavior is attributed to the specific conditions that allow the dispersed-phase thread to recede and stop within the outlet channel after pinch-off.

These findings may have significant implications for various applications of droplet microfluidics, including single-cell analysis, drug delivery, and advanced diagnostics. The discovery of the Bi-modal pattern, in particular, offers new opportunities for generating controlled distributions of droplet sizes without the need for additional active control elements. This breakthrough could potentially revolutionize fields that rely on droplet-based technologies, enabling sophisticated and precise manipulation of microscale fluid dynamics.

Acknowledgements

Tetuko Kurniawan acknowledges the support within the Preludium 23 grant (UMO-2024/53/ N/ST8/04010) from the National Science Centre, Poland. Paperpal and Claude Sonnet 4 were used to provide grammatical corrections and to generate suggestions for polishing the language.

References

1. Jammes F.C., Maerkl S.J., How single-cell immunology is benefiting from microfluidic technologies, *Microsystems and Nanoengineering*, **6**(1): 45, 2020.
2. Li B. *et al.*, Droplets microfluidics platform–A tool for single cell research, *Frontiers in Bioengineering and Biotechnology*, **11**: 1121870, 2023.
3. Kung C.-T. *et al.*, Microfluidic synthesis control technology and its application in drug delivery, bioimaging, biosensing, environmental analysis and cell analysis, *Chemical Engineering Journal*, **399**: 125748, 2020.
4. Mu H.-Y. *et al.*, Microfluidic-based approaches for COVID-19 diagnosis, *Biomicrofluidics*, **14**(6): 061504, 2020.
5. Yuan H. *et al.*, Microfluidic screening and genomic mutation identification for enhancing cellulase production in Pichia pastoris, *Biotechnology for Biofuels and Bioproducts*, **15**(1): 50, 2022.
6. Song H., Chen D.L., Ismagilov R.F., Reactions in droplets in microfluidic channels, *Angewandte Chemie International Edition*, **45**(44): 7336–7356, 2006.
7. Kaminski T.S., Garstecki P., Controlled droplet microfluidic systems for multistep chemical and biological assays, *Chemical Society Reviews*, **46**(20): 6210–6226, 2017.
8. Gu S.-Q. *et al.*, Multifunctional picoliter droplet manipulation platform and its application in single cell analysis, *Analytical Chemistry*, **83**(19): 7570–7576, 2011.
9. Bremond N., Thiam A.R., Bibette J., Decompressing emulsion droplets favors coalescence, *Physical Review Letters*, **100**(2): 024501, 2008.
10. Link D.R. *et al.*, Geometrically mediated breakup of drops in microfluidic devices, *Physical Review Letters*, **92**(5): 054503, 2004.
11. Chen Y. *et al.*, Three-dimensional splitting microfluidics, *Lab on a Chip*, **16**(8): 1332–1339, 2016.
12. Mazutis L., Griffiths A.D., Preparation of monodisperse emulsions by hydrodynamic size fractionation, *Applied Physics Letters*, **95**(20): 204103, 2009.
13. Hatch A.C. *et al.*, Passive droplet sorting using viscoelastic flow focusing, *Lab on a Chip*, **13**(7): 1308–1315, 2013.
14. Huebner A. *et al.*, Static microdroplet arrays: A microfluidic device for droplet trapping, incubation and release for enzymatic and cell-based assays, *Lab on a Chip*, **9**(5): 692–698, 2009.
15. Zaremba D., Blonski S., Korczyk P.M., Concentration on demand – A microfluidic system for precise adjustment of the content of single droplets, *Chemical Engineering Journal*, **430**: 132935, 2022.
16. Zaremba D., Blonski S., Korczyk P.M., Integration of capillary–hydrodynamic logic circuitries for built-in control over multiple droplets in microfluidic networks, *Lab on a Chip*, **21**(9): 1771–1778, 2021.

17. Sart S. *et al.*, Cell culture in microfluidic droplets, *Chemical Reviews*, **122**(7): 7061–7096, 2022.
18. Yao C. *et al.*, Two-phase flow and mass transfer in microchannels: A review from local mechanism to global models, *Chemical Engineering Science*, **229**: 116017, 2021.
19. Lee W., Walker L.M., Anna S.L., Role of geometry and fluid properties in droplet and thread formation processes in planar flow focusing, *Physics of Fluids*, **21**(3): 032103, 2009.
20. Cubaud T., Mason T.G., Capillary threads and viscous droplets in square microchannels, *Physics of Fluids*, **20**(5): 053302, 2008.
21. Joensson H.N., Andersson Svahn H., Droplet microfluidics—A tool for single-cell analysis, *Angewandte Chemie International Edition*, **51**(49): 12176–12192, 2012.
22. Korczyk P.M. *et al.*, Accounting for corner flow unifies the understanding of droplet formation in microfluidic channels, *Nature Communications*, **10**(1): 2528, 2019.
23. van der Walt S. *et al.*, scikit-image: image processing in Python, *PeerJ*, **2**: e453, 2014.
24. Harris C.R. *et al.*, Array programming with NumPy, *Nature*, **585**(7825): 357–362, 2020.
25. Kurniawan T., *Droplet Generation in Microfluidic Cross-Junctions: Mechanisms and Applications as Cell Incubators*, PhD Thesis, Institute of Fundamental Technological Research, Polish Academy of Sciences, 2025.
26. Garstecki P. *et al.*, Formation of droplets and bubbles in a microfluidic T-junction—scaling and mechanism of break-up, *Lab on a Chip*, **6**(3): 437–446, 2006.
27. Humphry K.J. *et al.*, Suppression of instabilities in multiphase flow by geometric confinement, *Physical Review E*, **79**(5): 056310, 2009.
28. Kurniawan T. *et al.*, Formation of droplets in microfluidic cross-junctions at small capillary numbers: Breakdown of the classical squeezing regime, *Chemical Engineering Journal*, **474**: 145601, 2023.